IEEE Access
Multidisciplinary | Rapid Review | Open Access Journal

Received January 28, 2019, accepted February 14, 2019, date of publication February 22, 2019, date of current version May 10, 2019.

Digital Object Identifier 10.1109/ACCESS.2019.2900376

Multi-Focus Image Fusion Based on Adaptive Dual-Channel Spiking Cortical Model in Non-Subsampled Shearlet Domain

SHUAIQI LIU[1,2], JIE WANG[1,2], YUCONG LU[1,2], HAILIANG LI[3], JIE ZHAO[1,2], AND ZHIHUI ZHU[4]

[1]College of Electronic and Information Engineering, Hebei University, Baoding 071000, China
[2]Machine Vision Engineering Research Center of Hebei Province, Baoding 071000, China
[3]Department of Electronic and Information Engineering, The Hong Kong Polytechnic University, Hong Kong
[4]Center of Imaging Science, Johns Hopkins University, Baltimore, MD 21218, USA

Corresponding author: Shuaiqi Liu (shdkj-1918@163.com)

This work was supported in part by the National Natural Science Foundation of China under Grant 61572063 and Grant 61401308, in part by the Natural Science Foundation of Hebei Province under Grant F2016201142, Grant F2018210148, and Grant F2016201187, in part by the Opening Foundation of Machine Vision Engineering Research Center of Hebei Province under Grant 2018HBMV02, in part by the Science Research Project of Hebei Province under Grant QN2016085, in part by the Natural Science Foundation of Hebei University under Grant 2014-303, in part by the Post-Graduate's Innovation Fund Project of Hebei University under Grant hbu2018ss01, and in part by the High-Performance Computing Center, Hebei University.

ABSTRACT To get a better fused performance in the multi-focus image fusion based on a transform domain, a new multi-focus image algorithm combined with the adaptive dual-channel spiking cortical model (SCM) in non-subsampled shearlet (NSST) domain and the difference images is proposed in this paper. First, a basic fused image is constructed in the NSST domain by registering the source image and adaptive dual channel SCM (dual-channel SCM). Next, the focus areas of the sources input images based on the difference images between the basic fused image and the sources images are detected. In the end, the final fused image generated in this paper is realized by combining the focal regions. Because of the global coupling of the dual-SCM, the synchronization characteristics of the pulse, and the multi-resolution and direction of the NSST, the proposed algorithm can preserve the information of the source's image well and present a clear image more in line with the human visual effects. In summary, the image fusion algorithm that we have designed is superior to the most advanced algorithms.

INDEX TERMS Difference images, multi-focus image fusion, non-subsampled shearlet, spiking cortical model.

I. INTRODUCTION

Image fusion technology mainly produces images that are more clearly and easily recognized by combining information of multiple images of the same object [1]. Because the original input images are limited in the focal length of the camera, they cannot reflect the panoramic scene. Therefore, compared with any single source image, the fused images are more used in machine learning and visual perception [2]. In general, multi-focus image fusion has three strategies: pixel-level information feature fusion, feature-level information feature fusion, and decision-level information feature fusion [3]. Pixel-level information feature image fusion methods are mainly divided into two different types: spatial domain algorithms and transform domain algorithms. Algorithms based on spatial domain include principal component analysis [4], [5], the algorithms based on guided filtering [6], image fusion algorithms based on similar features and human perception [7] and others. The fusion algorithms based on transform domain are primarily studied in the multi-resolution geometric analysis (MGA) tool domain and they can be divided into local energy function (for instance, wavelet-based image fusion algorithms in [8], ripplet-based image fusion algorithms in [9], contourlet-based image fusion algorithms in [10], shearlet-based image fusion algorithms in [11], image fusion algorithms based on trained dictionaries

The associate editor coordinating the review of this manuscript and approving it for publication was Jeon Gwanggil.

in [12] and [13], image fusion in discrete cosine transform domain in [14]) and artificial neural network (ANN) (such as contourlet with PCNN [15], shearlet (ST) with PCNN [16], contourlet with SCM [17]).

MGA tools have a good application in image fusion (for instance discrete wavelet transform (DWT), non-subsampled contourlet transform (NSCT), ST and others). In recent years, with simple calculation and image representation sparsely, contourlet transform has gained high value and achieved good results in image fusion methods [10], [15], [17]. However, contourlet transform is sensitive to shift-translation [18]. NSCT, constructed by non-subsampled directional filter and non-subsampled Laplacian transform, can overcome this drawback and NSCT-based image fusion method can achieve satisfied fusion result, but the computation intensive hinders its applications on real-time system. Compared with NSCT, ST [19], [20], with a rigorous mathematical framework and smaller support range of shear filter, is able to decrease the computation [21]. But ST also lacks shift-invariance, which will lead some artifacts on fusion processing. Later, in order to make better image fusion to make up for the deficiencies of NSCT and ST, scholars have proposed NSST [21], [22]. Compared to other MGA tools, NSST has better sparse representation ability with shift-invariance and less computation. In summary, image fusion based on NSST can achieve better fused performance.

However, because of nonlinear operations in the transform domain, fusion methods based on MGA tools also cause pixel distortion [7]. And fusion methods based on spatial domain or ANN with linear fusion technique can reduce pixel distortion [22]. PCNN is a simplified model which is suitable for implementing the synchronous pulse excitation characteristics. The excellent characteristics of PCNN make it widely used in a variety of image processing methods, such as image fusion processing, image denoising processing and image segmentation processing. However, the calculation intensity has a great influence on the implementation of PCNN-based image fusion processing [17], [22]. Image fusion methods based on traditional PCNN usually need complex calculations with lots of iterations. And multiple parameters should be to tune in the PCNN-based image fusion [23]. The dual-channel PCNN simplifies complex calculations on the basis of a single-channel PCNN, but there are still a lot of iterations and parameter adjustments. The simplified pulse coupled neural network (S-PCNN) [24], [25] is a simplified PCNN model by removing the external coupling and exponential decay characteristics of PCNN. Based on the single-channel S-PCNN, the dual-channel S-PCNN can simultaneously process the input pair of source images to produce results, further saving computation time. An intersecting critical model (ICM) was designed with more models (such as Hodgkin-huxley, FitHugh-Nagumo, and Eckhorn) [26]. The ICM has only two coupled oscillators, which can effectively reduce the calculation time and have higher real-time performance. ICM can better access real biological neurons, and better preserve the basic characteristics of neural networks. In order to have higher practical value in the application, a two-channel ICM is proposed, which has two stimuli to process a pair of source images at the same time, which makes the model more computationally efficient. However, the above model also requires more parameter adjustments in the image fusion processing. So, scholars have put forward many improved and simplified PCNN models to improve the performance of image fusion, and SCM is one of them with lower computation. SCM can be used in image fusion due to two features: one is that SCM, accords with Weber-Fechnerlaw, is tardy to high intensity stimulation but heavily sensitive to low intensity; the other is the time matrix of the SCM which can be regarded as be the perception of human subjective stimulus intensity [27]. SCM is highly utilized in image fusion, for instance, in [17] and [28], image fusion methods base on SCM and CT is proposed. And an effective medical image fusion based on rolling guidance filter and SCM is proposed in [29]. Though the above fusion algorithms have obtained good results, one SCM model has only one stimulus, in which case the entire image fusion process cannot be processed, so image fusion process usually needs multiple SCMs. Therefore, the application of standard SCM in image fusion has been structurally limited to a certain extent. Furthermore, in almost all fusion methods, synaptic linking weight of SCM is const. So, the synaptic linking weight cannot lead to the best image fusion performance [28].

Because the SCM model is a single channel, it is not possible to process a pair of source images directly. Inspired by the literature [30], we changed the original SCM model to a dual-channel SCM model, which is more conducive to images fusion. Compared to dual-channel PCNN, dual-channel S-PCNN and dual-channel ICM, it has fewer parameter settings and can effectively handle low-efficiency and computationally complex problems, resulting in the fused image that is more human-like. By combining the link strengths, the corresponding pixel gradients in the image are calculated throughout the model, and the iteration time is adaptively determined by the time matrix. As all we know, it is the first time that dual-channel SCM model is proposed and applied to image fusion. And both source images are simultaneously input into the same SCM conveniently. More importantly, this set of parameters can automatically achieve the excellent performance of the fusion during the running of the algorithm, which also helps to suppress image distortion in image fusion based on shearlet domain. If you want to process many images at the same time, you can cascade to produce the final result.

Taking into account the characteristics of MGA tools and dual-SCM, we can intuitively draw the following conclusions. Firstly, NSST has great advantages over other MGA tools and it is also widely used in the image processing. Secondly, adaptive dual-SCM can effectively suppress the image distortion caused on MGA fusion method. As a result, we harbor advantages of NSST as well as dual-SCM and then designed a multi-focus image fusion method by

combining these two methods. The method designed in this paper can obtain better image visual effects, because it can more effectively pick up the details of focused region in the source images. However, the fired map of ANNs (PCNN or SCM) may be discontinuous [23]. Inspired by the method in [31], we refined the based fused image by using the salient features of the difference images between the basic fused image and the original input images.

As we all know, the fused algorithms based on deep learning has achieved good experimental results recently. In [32], image segmentation-based multi-focus image fusion through multi-scale convolutional neural network (MSCNN) is proposed, which is a novel image segmentation-based multi-focus image fusion algorithm. MSCNN achieves segmentation through a multi-scale convolutional neural network, which performs a multi-scale analysis on each input image to derive the respective feature maps. Afterward, the fused map is post-processed using initial segmentation, morphological operation, and watershed to obtain the segmentation map and decision map, which can achieve an optimum fusion performance in light of both qualitative and quantitative evaluations. Liu *et al.* [33] propose multi-focus image fusion with a deep convolutional neural network (CNN). CNN for image fusion in this algorithm is trained for images of different degrees of clarity for the image fusion process. From the trained CNN, the focused map can be obtained directly. Tang *et al.* [34] propose pixel convolutional neural network for multi-focus image fusion(P-CNN). P-CNN can identify the focus and defocus pixels in the image according to the neighborhood information. The distinction for pixels is based on a set of training images in a public image database. Guo *et al.* [35] propose fully convolutional network-based multi-focus image fusion (FCNN) based on the method in [33]. The pooling layer of the CNN model in the [33] is replaced by a convolutional layer, and a new model is generated for multi-focus image fusion. Then, through the backward propagation residual, the parameters of each layer of the CNN are updated layer by layer. In these deep learning algorithms, the original images are processed by different models, and a good visual effect is obtained, but the training of CNN is time consuming. In these models, a large number of data sets need to be trained, and the convolutional layer as feature extraction is time consuming in the running process. It is proposed in [36] that the current fusion method based on deep learning has challenges in network architecture design and network training dataset generation. And the image fused algorithm designed in this paper is more efficient and does not require training data sets. NSST can divide images into more detailed information features of different frequencies and directions. The dual-channel SCM can process the source images at the same time, which simplifying the calculation process and enabling better application and engineering.

The structure of the article is divided into the following sections. In the second section, we introduce the basic knowledge of NSST structure. In the third section, we give the construction of SCM and its improvement. In the fourth section, we introduce the workflow of the novel fusion algorithm by using dual-SCM in NSST domain with difference images. In the fifth section, we give the comparison experimental results between the proposed algorithm and other representative fusion algorithms. Finally, we draw some conclusions in the last section.

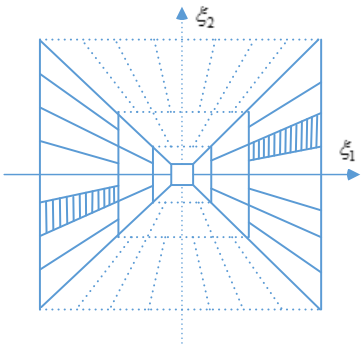

FIGURE 1. The tiling of the frequency plane formed by the ST.

II. NON-SBUSAMPLED SHEARLET TRANSFORM

ST is a new multi-scale geometric analysis algorithm by using the construction of composite wavelets. And it overcomes the disadvantages of contourlet and curvelet transform [18], [20]. In the case, $n = 2$, the shearlet functions are generated by affine transform as following [17], [19]:

$$\Omega_{\boldsymbol{AB}}(\psi) = \left\{ \begin{array}{l} \psi_{j,l,\boldsymbol{k}}(\boldsymbol{x}) = |\det \boldsymbol{A}|^{j/2} \psi\left(\boldsymbol{B}^l \boldsymbol{A}^j \boldsymbol{x} - \boldsymbol{k}\right) \\ : j, l \in Z, \boldsymbol{k} \in Z^2 \end{array} \right\}, \quad (1)$$

where $\psi \in L^2(R^2), \boldsymbol{A}, \boldsymbol{B}$ are 2×2 invertible matrices and $|\det \boldsymbol{B}| = 1$. The dilations $\boldsymbol{A}^j$ are telescopic transform matrices, while the matrices $\boldsymbol{B}^l$ are related to geometric transform of the preservative region, such as rotations and shear [19]–[21]. Normally $\boldsymbol{A} = \boldsymbol{A}_0 = \begin{pmatrix} 4 & 0 \\ 0 & 2 \end{pmatrix}$ represents the anisotropic dilation matrix, and $\boldsymbol{B} = \boldsymbol{B}_0 = \begin{pmatrix} 1 & 1 \\ 0 & 1 \end{pmatrix}$ represents shear matrix in formula (1). Then, the NSST decomposition is constructed as shown in FIGURE 1.

From FIGURE 2, we can know that the shearlet function $\hat{\psi}_{j,l,\boldsymbol{k}}$ is supported on a pair of trapezoids of approximate size $2^{2j} \times 2^j$. And the slope of the trapezoids is $l2^{-j}$.

If $f \in L^2\left(R^2\right)$, the continuous ST can be represented as the following.

$$SH_\psi = \langle f, \psi_{j,l,\boldsymbol{k}} \rangle, \quad (2)$$

where $j \geq 0, l = -2^j, 2^j - 1, \boldsymbol{k} \in Z^2$.

NSST [20], [22] is realized through different scales and directions. First of all, the image is decomposed by Nonsubsampled pyramids (NSP). It can be concluded by scale decomposition that NSP can generate k high frequency subband coefficients and one low frequency sub-band coefficients after k-th scale decomposition. In the second part,

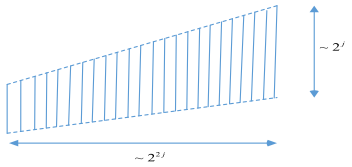

FIGURE 2. The frequency support of ST.

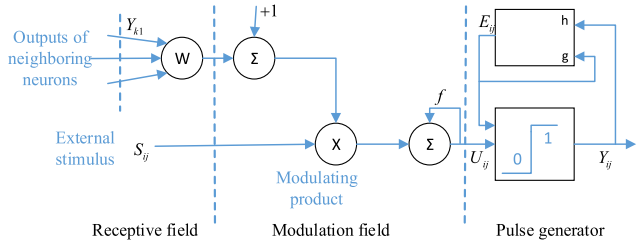

FIGURE 3. SCM structure of model.

the shear filter is applied to achieve multi-direction transformation. The standard shear filter is effectuated in a pseudo-polarized grid through translating the window function, whereas NSST maps the filter to Cartesian coordinate system. This approach avoids the down-sampling operation and thus satisfying the translation invariance [20].

III. ADAPTIVE DUAL-CHANNEL SPIKING CORTICAL MODEL

In this section, we first briefly review the original SCM, and then propose a new adaptive dual-SCM model that can directly give the fusion result. Compared with SCM, the linking input of adaptive dual-SCM model is improved, and the parameter values can be adaptively selected, e.g. linking strength and iteration amount.

A. SPIKING CORTICAL MODEL

Jin *et al.* [24] proposed the SCM model based on Eckhorn's model, which is consistent with visual characteristic. Indeed, many effective fusion methods working for different kinds of images are proposed [17], [23], [28], [29]. From FIGURE 3, we can see that, each neuron comprises three components in the SCM: receptive field, modulation field, and pulse generator.

As can be seen from FIGURE 3, the he indexes i and j indicate the locations of the pixel of image. k and l represent the locations of their adjacent pixels respectively, and n represents the time of the current repeated feedback process. We can compute the receiving and linking field and modulating product as following.

$$U_{ij}(n) = fU_{ij}(n-1) + S_{ij}\sum_{kl} W_{ijkl}Y_{kl}(n-1) + S_{ij}, \quad (3)$$

where $U_{ij}(n)$ represents the internal activity and f represents the attenuation coefficient factor of $U_{ij}(n)$. S_{ij} represents the external stimulus of this model. W_{ijkl} represents the weight of

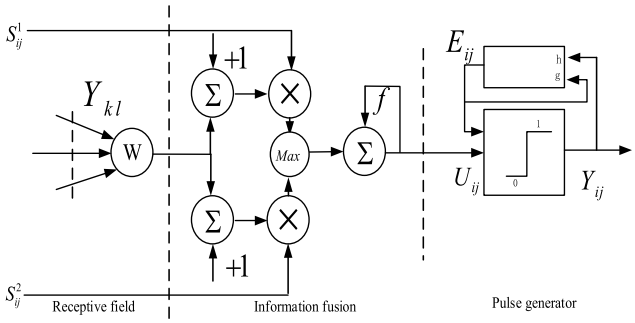

FIGURE 4. The dual-channel SCM model.

synaptic linking in this model, and $Y_{kl}(n-1)$ represents the former output pulse of this model.

The firing events in SCM model are determined by the pulse generator in formula (4). And the output pulse Y_{ij} can be calculated by internal activity and dynamic threshold as following.

$$Y_{ij}(n) = \begin{cases} 1 & if\ 1/(1+\exp(U_{ij}(n) - E_{ij}(n))) > 0.5 \\ 0 & otherwise, \end{cases} \quad (4)$$

The pulse threshold range for each neuron is determined by the following.

$$E_{ij}(n) = gE_{ij}(n-1) + hY_{ij}(n-1), \quad (5)$$

where g represents the attenuation coefficient and h represents the threshold magnitude coefficient.

When image processing is performed, the pixels of the original input image in the SCM rational model are closely related to the number of neurons, and they correspond to each other. This makes the image more convenient, reasonable, and easy to implement during the fusion process.

B. DUAL-CHANNEL SPIKING CORTICAL MODEL

Undoubtedly, there requires more than one SCM model for image fusion based on SCM, which makes the method complex and time-consuming. Obviously, only one stimulus for each neuron is an obstacle for multiple-image fusion based on SCM. To overcome these defects of single-channel SCM for image fusion, inspired by these characteristics in the dual PCNN model in [29], we propose a new SCM model—dual-channel SCM model. And compared to the dual PCNN model, the dual S-PCNN model and the dual ICM model, where the dual channel SCM has fewer parameters, this makes the calculation process easier. The model presented in this paper is shown in FIGURE 4.

Each dual-channel SCM contains three components: receptive field, the information fusion structure of the image and the pulse generator part. Surrounding neuron stimulus and external stimulus as two kinds of inputs are obtained in the receptive area. The fused image is stored in information fusion part, while the pulse generator part launches output pulses. In dual-SCM, we simultaneously input both stimuli into the model, and then we can get the fused image of the

TABLE 1. Runtime of different dual-channel models.

The fusion model	Time(s)
dual-channel PCNN	45.0224
dual-channel S-PCNN	42.2416
dual-channel ICM	40.4522
dual-channel SCM	30.7034

dual-SCM output. And we can describe the mathematical equations of dual-SCM as follows.

$$U_{ij}(n) = fU_{ij}(n-1) + \max\left\{\begin{matrix} S_{ij}^1\left(\sum_{kl} W_{ijkl}Y_{kl}(n-1)+1\right), \\ S_{ij}^2\left(\sum_{kl} W_{ijkl}Y_{kl}(n-1)+1\right)\end{matrix}\right\}, \quad (6)$$

$$E_{ij}(n) = gE_{ij}(n-1) + hY_{ij}(n-1), \quad (7)$$

$$Y_{ij}(n) = \begin{cases} 1 & if\ 1/(1+\exp(U_{ij}(n) - E_{ij}(n))) > 0.5 \\ 0 & otherwise, \end{cases} \quad (8)$$

where $U_{ij}(n)$ represents the internal activity. And the decision map of the fused image can be determined by $U_{ij}(n)$. S_{ij}^1 and S_{ij}^2 represent the external stimulus of the two input sources images accordingly. The rest parameters in dual-channel SCM have the same meaning to the parameters in SCM.

The most striking feature of dual-SCM is that two original images can be are simultaneously input into this model to obtain the desired image. From the output of dual-SCM, we can get the fused image directly. So, the fused processing can be finished conveniently and quickly. Dual-SCM can also have the characteristics of global coupling and pulse synchronization just like SCM, and make full use of local image information, which is more conducive to image fusion.

To show the advantages of the dual-channel SCM model, we compare it to dual-channel PCNN, dual-channel S-PCNN, and dual-channel ICM in the fused effect. In the experimental, we set the iteration time to 200, and the fusion strategy is maximining the absolute value of the fire time. In FIGURE 5 and TABLE 1, we present experimental results and computational efficiencies for different dual-channel models. It can be seen that the dual-channel SCM can better distinguish the focused and unfocused regions of the image in the decision map, and has higher computational efficiency.

C. ADAPTIVE PARAMETERS SETTING IN DUAL-SCM

In dual-SCM, the number of parameters that need to be set is only five in total, including f, W_{ijkl}, g, h and n. Among them, f, g and h are constants that can be easy to be determined. In our paper, these parameters are the same to [29], that is, f can be assigned by the value 0.7, and g can be assigned by the value 0.8, and h can be assigned by the value 20.

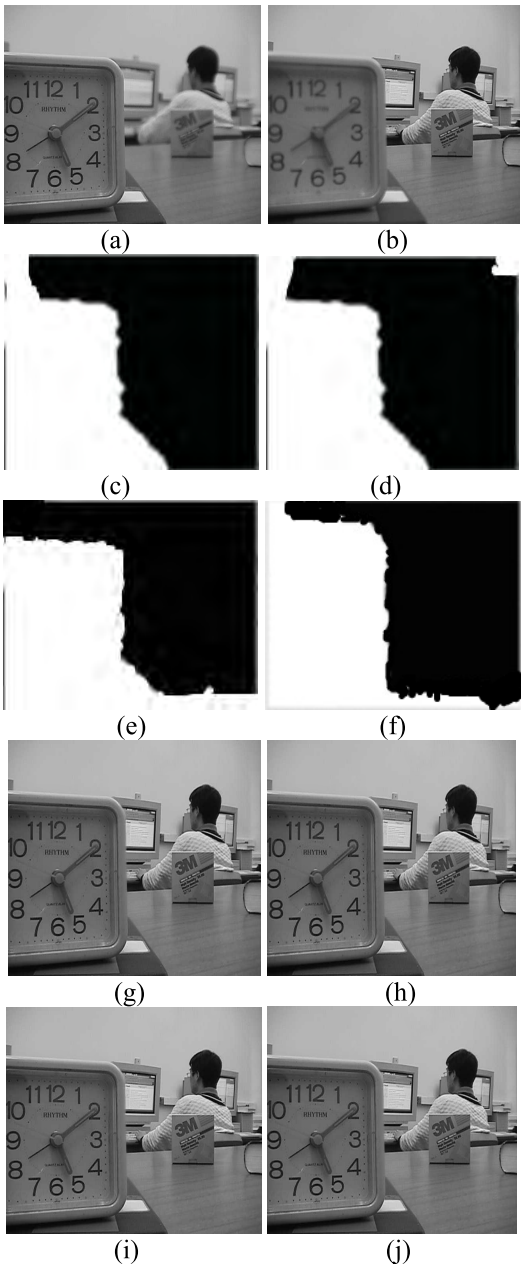

FIGURE 5. The performance of different dual-channel models. (a) left focu source image, (b) right source image, and (c)-(f) are decision maps for a two-channel PCNN, dua-channel S-PCNN, dual-channel ICM, and dual-channel SCM. (g)-(j) are dual channel PCNN, dual channel S-PCNN, dual channel ICM and dual channel SCM fusion results.

The parameters W_{ijkl} and n are important for image fusion. So, we use the sum-modified-Laplacian (SML) of the images to adaptively obtain the synaptic linking weight W_{ijkl}. And the iteration value n can be de determined adaptively by time matrix of the images.

In our opinion, the synaptic linking weight should be related to the clarity of source images. An adaptive synaptic linking weight is defined by using SML of the source images. That is,

$$W_{ij} = \max\left\{SML\left(I_1\left(i,j\right)\right), SML\left(I_2\left(i,j\right)\right)\right\}, \quad (9)$$

FIGURE 6. The fired time map, the largest value is 18.

In a general case, we assume that I_1 and I_2 are the source images in image fusion and external stimulus S_{ij} also can be represented by SML of the source images. That is,

$$S_{ij} = SML\left(I\left(i,j\right)\right), \tag{10}$$

SML reflects can properly reflect the focusing characteristics and clarity of the image to some extent [14]. In order to obtain a fused image with better visual characteristics and richer and more prominent details, we use SML as the synaptic linking weight of dual-SCM. The SML at the pixel (i,j) can be calculated as following:

$$SML\left(I(i,j)\right) = \sum_{(x,y)\in\omega_{(i,j)}} \left[ML\left(I(x,y)\right)\right]^2, \tag{11}$$

where $\omega_{(i,j)}$ denotes a rectangular window with sizes 3×3 which is centered on pixel (i,j). For $\forall\,(x,y) \in \omega_{(i,j)}$, we have the follow definition,

$$\begin{aligned} &ML\left(I\left(x,y\right)\right) \\ &\quad = \left|2I(x,y) - I(x-step,y) - I(x+step,y)\right| \\ &\qquad + \left|2I(x,y) - I(x,y-step) - I(x,y+step)\right|, \end{aligned} \tag{12}$$

where *step* represents an alterable distance between pixels. Here, we select variable *step* with a value of 1.

Generally speaking, in image processing, the iteration number n in SCM is hard to determine. Most scholars determine n through experiments or experience. Zhan *et al.* [27] and Liu *et al.* [29] selected the iteration number n of SCM with a value of 40. As we all know, if n is too large, the processing time will be too long, and if the value of n is too small, SCM will not take taken full advantages of to get optimal image processing effect, which means the synchronous impulse characteristics of SCM are not well applied to the image fusion process. Being inspired by [30], the iteration number can be fixed by the time matrix T. Then, T is represented by the following formula:

$$T_{ij}\left(n\right) = \begin{cases} n, & if\ Y_{ij}(n) = 1 \\ T_{ij}\left(n-1\right), & otherwise, \end{cases} \tag{13}$$

where $T_{ij}\left(n\right)$ denotes first firing time of each neuron. FIGURE 6 show the fired time map by equation (13).

In the source image, the pixels with similar image intensity values tend to have the same or similar firing time, so the dual-SCM can get time information of each neuron as well as retain space information. These advantages of dual-SCM are obviously very helpful to image fusion. From the definition of T, we can conclude that, $T_{ij}\left(n\right)$ is assigned to n if the neuron fires for the first time at the time of n, while $T_{ij}\left(n\right)$ is assigned to zero when the neuron has never fired. In Adaptive dual-SCM, the iteration will stop when each element value of T is nonzero, which means all neurons have been fired adaptively.

IV. IMAGE FUSION BASED ON DUAL-SCM IN NSST DOMAIN

Since NSST has the properties of multi-scale decomposition and shift invariant, we use NSST to decompose the source images in the proposed image fused algorithm. Whether for low-frequency or high-frequency coefficients of NSST, SML of NSST coefficients is a better regional energy function representation on the image edge details [9], so better image fusion effect can be archived by dual-SCM motivated by SML, as shown in FIGURE 7 (The image fusion framework according to SCM is the same to fused method in [37], and the fused method named SML-SCM just replace the inputs and synaptic linking weight by using SML in source images. In FIGURE 7, we provide two sets of original images. The first group is medical images of CT and MRI, and the second group is clock images of left focus and right focus. It is clear to see in image zooming). The final fused image needs to be further refined to complement the fused image based on the difference image, giving it more prominent detail and better visual effects.

The image fusion algorithm (NSST-SCM) proposed in this paper is specifically explained below. In a general case, we assume that I_1 and I_2 are two sources images whose focus is different.

Firstly, we can get the decomposition coefficients $C_{I_1}^{l,\theta}\left(i,j\right)$ and $C_{I_2}^{l,\theta}\left(i,j\right)$ of image I_1 and I_2 by NSST. And l denotes the scale in the NSST decomposition, while θ denotes direction of decomposition in the l-th scale in the coefficients of NSST. And if l is zero, $C_{I_1}^{l,\theta}\left(i,j\right)$ and $C_{I_2}^{l,\theta}\left(i,j\right)$ denote low frequency coefficients of image I_1 and I_2, otherwise they denote high frequency coefficients.

Secondly, SML of coefficients of NSST is computed by equation (11). $SML_{I_1}^{l,\theta}$ denotes SML of $C_{I_1}^{l,\theta}\left(i,j\right)$ and $SML_{I_2}^{l,\theta}$ denotes SML of $C_{I_2}^{l,\theta}\left(i,j\right)$. We normalize the SML of the NSST coefficients and take them as the stimuli for the inputs of dual-SCM, respectively. Running the equation (6-8) and (13), the dual-SCM can be finished when each element value of the time matrix is not zero. And we can get

$$\begin{cases} U_{ij}^{I_1}\left(n\right) = fU_{ij}\left(n-1\right) + SML_{I_1}^{l,\theta}\left(\sum_{kl} W_{ijkl}Y_{kl}\left(n-1\right) + 1\right) \\ U_{ij}^{I_2}\left(n\right) = fU_{ij}\left(n-1\right) + SML_{I_2}^{l,\theta}\left(\sum_{kl} W_{ijkl}Y_{kl}\left(n-1\right) + 1\right), \end{cases} \tag{14}$$

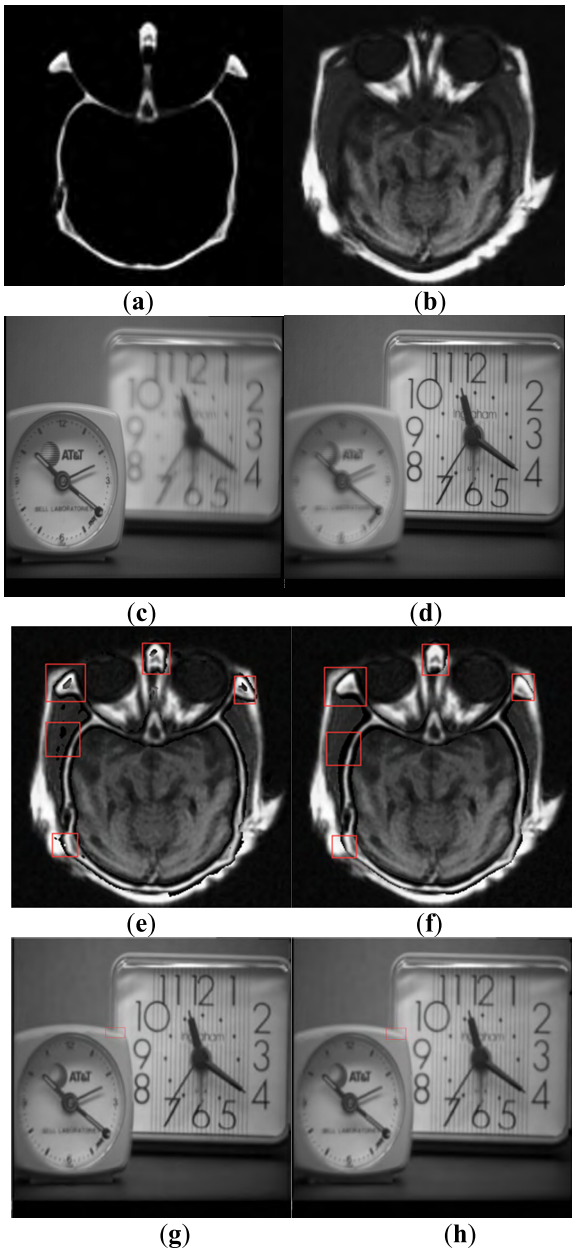

FIGURE 7. The performance of SML in SCM. (a) CT source image, b) MRI source image, c) left focu source image, d) right focus source image, (e, g) the SCM based fused images, (f,h) the SML-SCM based fused image.

where $U_{ij}^{I_1}(n)$ and $U_{ij}^{I_2}(n)$ represent the internal situation of the neuron of source images, respectively. Then, the fused NSST coefficients $C_F^{l,\theta}(i,j)$ are derived from

$$C_F^{l,\theta}(i,j) = \begin{cases} C_{I_1}^{l,\theta}(i,j) & if\ U_{ij}(N) = U_{ij}^{I_1}(N) \\ C_{I_2}^{l,\theta}(i,j) & if\ U_{ij}(N) = U_{ij}^{I_2}(N), \end{cases} \tag{15}$$

where N is the sum of each fire times.

Though inverse NSST, we can get the basic fused image F_b. Generally speaking, the pixels of F_b are pixels whose focus are the clearer ones in I_1 and I_2. So the signs of difference of F_b and I_1 or I_2 can tell us whether the fused image has image distortion or holes (see details in [31]). In this paper, $DiffF_{I_1}(i,j)$ and $DiffF_{I_2}(i,j)$ represent difference images by F_b minus I_1 and I_2, that is,

$$\begin{cases} DiffF_{I_1}(i,j) = F_b(i,j) - I_1(i,j) \\ DiffF_{I_2}(i,j) = F_b(i,j) - I_2(i,j), \end{cases} \tag{16}$$

It is evident that the regions with no evident gradient in the difference images correspond to the focused regions in the source images [31]. The obvious characteristics of the focused regions can be seen from the gradient characteristics of the differential images to some extent. Same as in [31], the level of activation in the original images can be measured by the gradient feature in the difference images. The energy of the gradient (EOG) of each pixel can well reflect the focus level of the fused image. And the higher the gradient energy is, the higher the focus level is. On the other hand, EOG can detect the edge information of the image and reduce the image duplication effectively. In our paper, we also use EOG to evaluate the focus levels of the fused image, and the EOG of each pixel can be calculated as follows [31]:

$$EOG(i,j) = \sum_{m=-\frac{1}{2}(M-1)}^{\frac{1}{2}(M-1)} \sum_{n=-\frac{1}{2}(M-1)}^{\frac{1}{2}(M-1)} \times \left(\left(I^{i+m}\right)^2 + \left(I^{j+n}\right)^2 \right), \tag{17}$$

where $\begin{cases} I^{i+m} = I(i+m+1,j) - I(i+m,j) \\ I^{j+n} = I(i,j+n+1) - I(i,j+n). \end{cases}$

As we all know, average filter can suppress blocking artifacts in the image, while median filter can remove the isolated points in the image. In our paper, different to using morphological filtering in [31], we use average filtering and median filtering to refine EOG of difference images. What's more, this refined technology based on average filtering and median filtering is more efficient than sliding window technique and morphological filtering. The difference images can be refined as follows.

$$EOG_{I_1,refined}(i,j) = Median\left(Average\left(EOG_{I_1}(i,j), M_1\right), M_2\right), \tag{18}$$

$$EOG_{I_2,refined}(i,j) = Median\left(Average\left(EOG_{I_2}(i,j), M_1\right), M_2\right) \tag{19}$$

where $EOG_{I_1}(i,j) = EOG\left(DiffF_{I_1}(i,j)\right)$ and $EOG_{I_2}(i,j) = EOG\left(DiffF_{I_2}(i,j)\right)$, $Average(\bullet)$ represents the average filter function, and $Median(\bullet)$ represents the median filter function, $M_1 \times M_1$ is the window size of average filter, while $M_2 \times M_2$ is the window size of median filter. In our algorithm, through experimental verification, M is set to 3, M_1 is set to 5 and M_2 is set to 7.

As the above shown, our fusion strategy map is determined based on the EOG of the difference image pixels. When the EOG of the different difference images pixels have a small value, it indicates that the difference between the fused image and the original images are small, that is, the pixel of the original images has a better focus level and serves as the pixel value of the final fused image. The selected pixel is

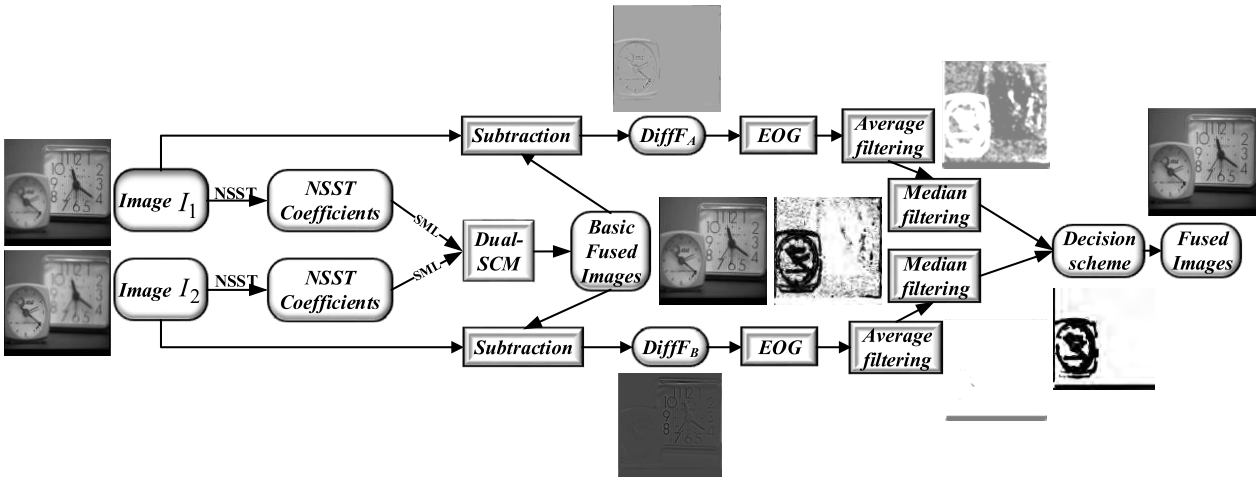

FIGURE 8. Flow chart of NSST-SCM based image algorithm.

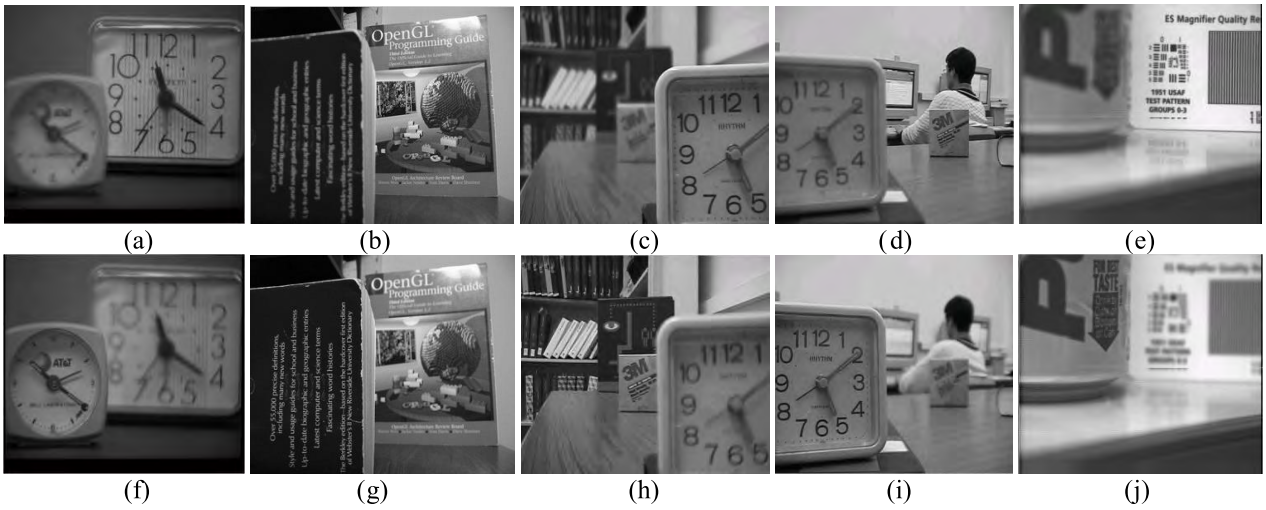

FIGURE 9. Different images to fuse.

from the pixel value of the source images I_1 or I_2, and the value from the source image A or B is regarded as 0 or 1 in the decision maps, respectively. Combining with different images, the final fused result is shown in the following formula:

$$F(i,j) = \begin{cases} I_1(i,j) if\ EOG_{I_1,refined}(i,j) < EOG_{I_2,refined}(i,j) \\ I_2(i,j) if\ EOG_{I_1,refined}(i,j) \geq EOG_{I_2,refined}(i,j), \end{cases} \tag{20}$$

In summary, the flow chart of the method we designed is given in FIGURE 8. First, a set of multi-focus images I_1 and I_2 are input, which are respectively decomposed by NSST to generate sub-band coefficients of different frequencies and directions. The decomposed coefficients are then processed by SML as synaptic connection weights for the dual-channel SCM inputs. The decomposed coefficients are processed by the dual-channel SCM to generate fusion coefficients of different frequencies and directions, and finally the inverse NSST transform is used to generate the initial fused image. In order to improve the fusion effect of the basic fused image, we further refined the decision map by the difference images between the basic fused image and source images.

V. EXPERIMENTAL RESULTS

A. COMPARISON OF DIFFERENT ALGORITHMS IN GRAY IMAGES

We first introduce several objective criteria to measure the performance of fusion algorithms, such as: objective criteria based on human perceptual inspiration quality indicators (Q_C) [40], image similarity based measures (Q_Y) [41], phase congruency-based fusion metric (Q_{PC}) [41], nonlinear correlation information entropy (Q_{NE}) [41], structural similarity-based fusion metric (Q_W) [41], edge information similarity measurement ($Q_{AB/F}$) [15], pixel level image fusion index (Q_{PL}) [41]. These indicators are used to represent the image fusion quality of different algorithms from different image

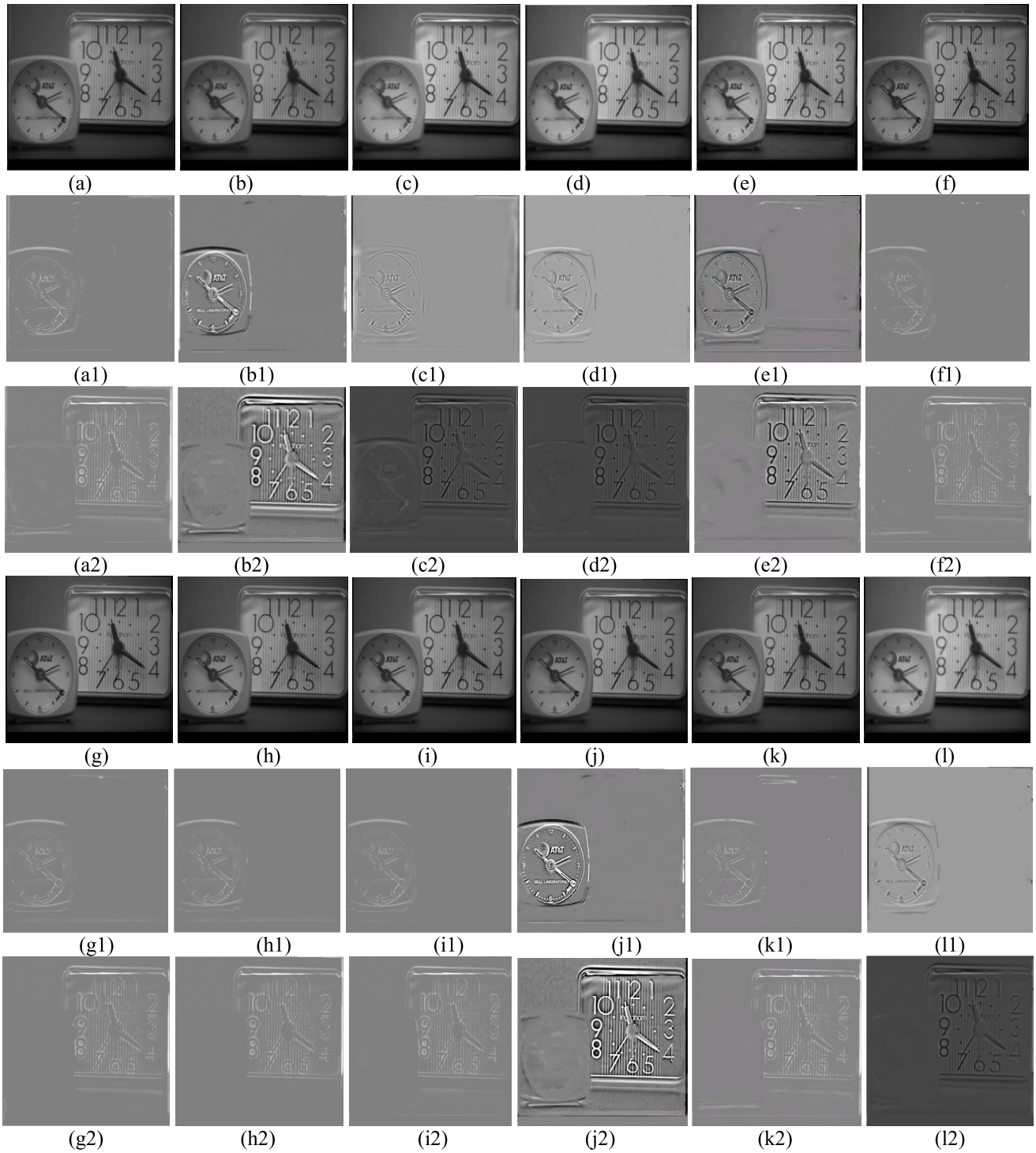

FIGURE 10. The fused performance of group a. (a-l) are the results of fusion images based on GFF, CST-GF, NSCT-PCNN, NSCT-SCM, NMF-DF, DCT, DSIFT, BF, CNN SSDI, P-CNN and NSST-SCM. And (a1,a2),(b1,b2),(c1,c2),(d1,d2),(e1,e2),(f1,f2),(g1,g2), (h1,h2),(i1,i2),(j1,j2,k1,k2),(l1,l2) are difference images (fused image minus figure (a) and (f)).

structure information. Normally, the larger the value of these seven objective evaluations is, the better the image fusion performance has. At the same time, we give the running time of different algorithms to compare the computational efficiency.

In order to evaluate the algorithm designed in this paper, we give the experimental results of different algorithms for comparison, as shown in FIGURE 9-14. FIGURE 9 give five pairs of images as the sources images to be tested all the fused algorithms. FIGURE9 (a) and (f) as group a are

FIGURE 11. The fused performance of group b. (a-j) are the results of fusion images based on GFF, CST-GF, NSCT-PCNN, NSCT-SCM, NMF-DFDCT,DSIFT,BF,CNN, SSDI, P-CNN and NSST-SCM. And (a1,a2),(b1,b2),(c1,c2),(d1,d2),(e1,e2),(f1,f2),(g1,g2),(h1,h2),(i1,i2), (j1,j2),(k1,k2),(l1,l2) are difference images (fused image minus figure 9 (b) and (g)).

clock images which includes different focus areas on the left and right. Group b contains FIGURE 9 (b) and (g), and they are book images with different focus. Group c contains FIGURE 9 (c) and (h), and they are disk images with different focus. Group d contains FIGURE 9 (d) and (i), and they are lab images with different focus. Group e contains FIGURE 9 (e) and (j), and they are pepsi images with different focus.

Comparison studies are performed in the experiments by using the following algorithms. (1) Image fusion process-

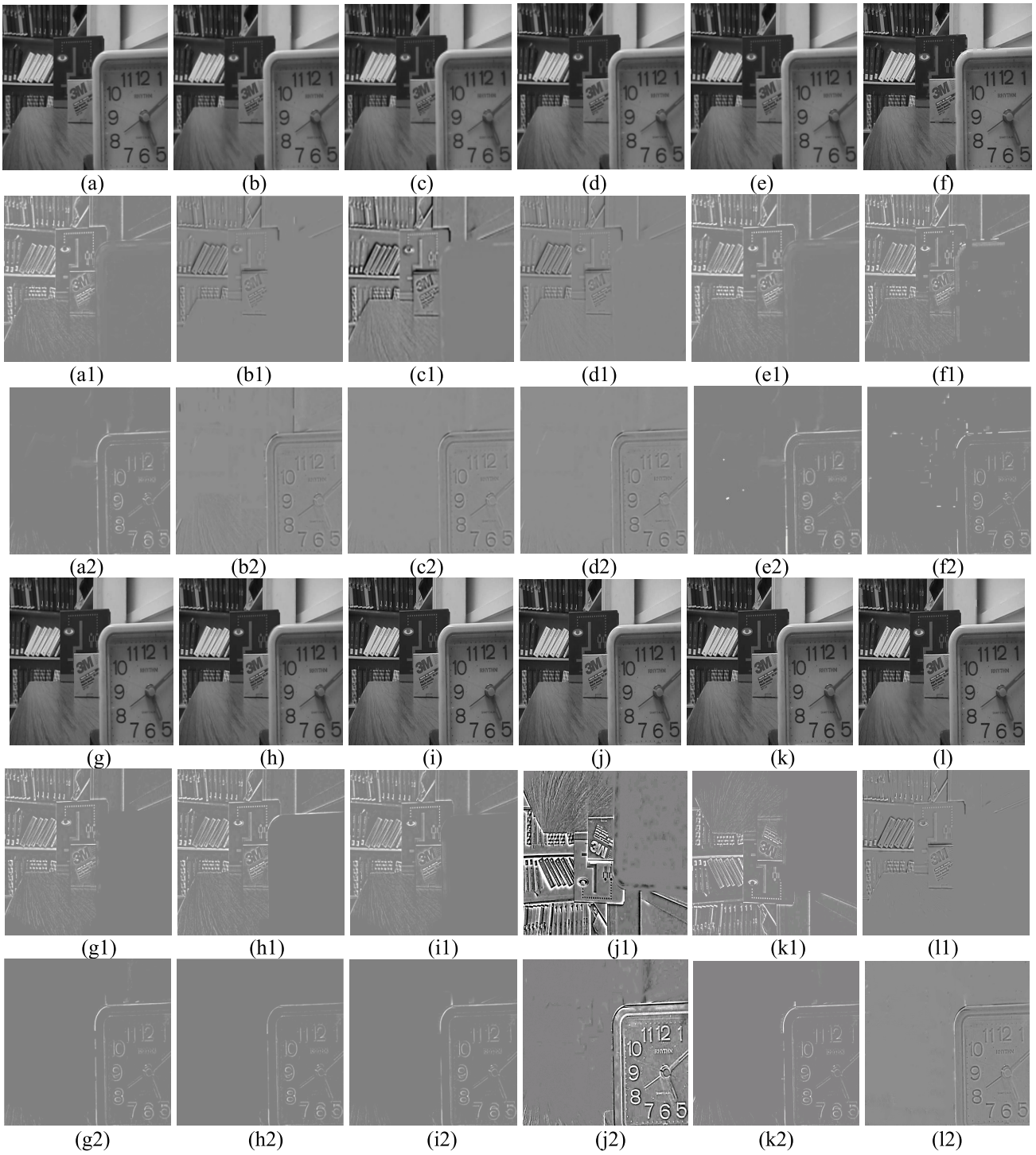

FIGURE 12. The fused performance of group c. (a-j) are the results of fusion images based on GFF, CST-GF, NSCT-PCNN, NSCT-SCM, NMF-DF, DCT,DSIFT,BF,CNN,SSDI, P-CNN and NSST-SCM. And (a1,a2),(b1,b2),(c1,c2),(d1,d2),(e1,e2),(f1,f2),(g1,g2), (h1,h2),(i1,i2),(j1,j2),(k1,k2),(l1,l2) are difference images (fused image minus figure (c) and (h)).

ing with guided filtering proposed in [7] (GFF). (2) Image fusion by using guided filtering in complex-shearlet domain proposed in [38] (CST-GF). (3) Image fusion algorithm by using spatial frequency-motivated PCNN in NSCT domain proposed in [15] (NSCT-PCNN). (4) Multi-focus image fusion by using SCM in NSCT domain proposed in [17] (NSCT-SCM). (5) Multi-focus image fusion algorithm by using non-negative matrix factorization and refined by difference images proposed in [31] (NMF-DF). (6) Multi-focus image fusion in DCT domain using variance and energy

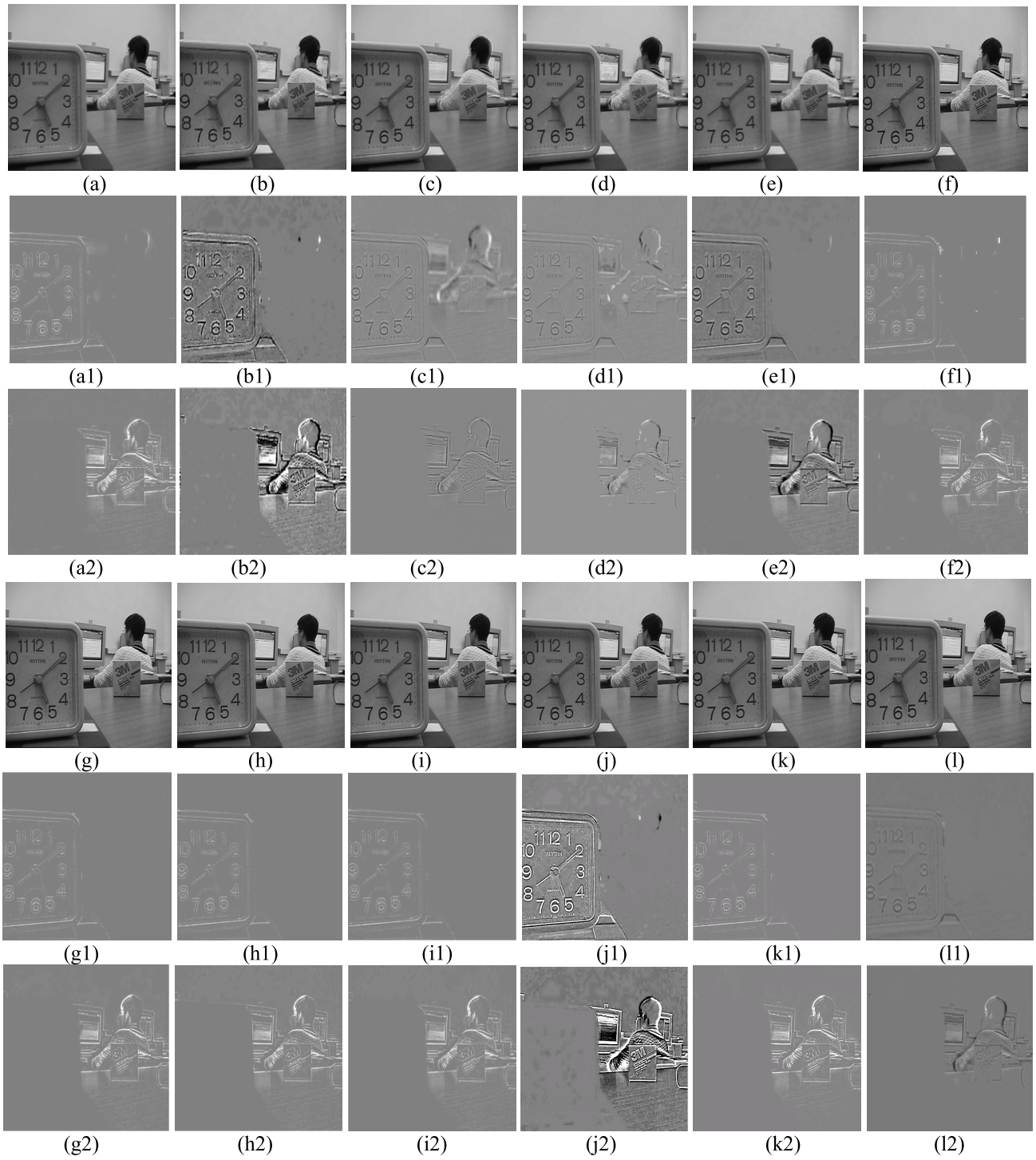

FIGURE 13. The fused performance of group d. (a-m) are the results of fusion images using GFF, CST-GF, NSCT-PCNN, NSCT-SCM, NMF-DF, DCT,DSIFT,BF,CNN,SSDI,P-CNN and NSST-SCM. And (a1,a2),(b1,b2),(c1,c2),(d1,d2),(e1,e2),(f1,f2),(g1,g2),(h1,h2),(i1,i2),(j1,j2), (k1,k2),(l1,l2) are difference images (fused image minus figure 9 (d) and (i)).

of Laplacian and correlation coefficient for visual sensor networks in [42] (DCT). (7) Multi-focus image fusion with dense SIFT in [43] (DSIFT). (8) Boundary finding based multi-focus image fusion through multi-scale morphological focus-measure in [44] (BF). (9) Multi-focus image fusion with a deep convolutional neural network in [33] (CNN). (10) High quality multi-focus image fusion using self-similarity and depth information in [7] (SSDI). (11) Pixel convolutional neural network for multi-focus image fusion in [34] (P-CNN). To be fair, the parameters of the comparison

FIGURE 14. The fused performance of group e. (a-j) are the results of fusion images using GFF, CST-GF, NSCT-PCNN, NSCT-SCM, NMF-DF, DCT,DSIFT,BF,CNN,SSDI, P-CNN and NSST-CM. And (a1,a2),(b1,b2),(c1,c2),(d1,d2),(e1,e2),(f1,f2),(g1,g2),(h1,h2),(i1,i2),(j1,j2), (k1,k2),(l1,l2 are difference images (fused image minus figure 9 (e) and (j)).

algorithms are selected based on the paper reported by the authors to obtain the best fusion results. The decomposition level of NSST is 2, with 2, 32 directions. In addition, the fused algorithms are realized and assessed by using MATLAB codes on Intel Core2 2.6 GHz machines which has a 4 GB RAM.

The methods above are respectively employed to fuse five group test images in FIGURE 9. FIGURE 10-14 show fused images and the difference images between sources images and fused image by using each fused algorithm.

As shown in the results of FIGURE 10 (a)-(l), it is easy to find that blocking effect and unexpected image degradation

TABLE 2. Ealuation indexes of different fusion algorithms in figure 10.

The fusion algorithm	Q_C	Q_Y	Q_{PC}	Q_{NE}	Q_W	$Q_{AB/F}$	Q_{PL}	Time(s)
GFF	9.1241	0.9894	0.7112	0.8132	0.6923	0.7232	0.5632	0.7778
CST-GF	9.2112	0.7134	0.7120	0.8241	0.6856	0.7524	0.5763	10.5641
NSCT-PCNN	8.9987	0.9653	0.7188	0.8347	0.7125	0.6775	0.6124	255.3342
NSCT-SCM	9.9132	0.9752	0.7184	0.8236	0.7253	0.7123	0.5832	195.4481
NMF-DF	9.3216	0.9734	0.7125	0.8564	0.6584	0.7341	0.5699	10.8821
DCT	9.4338	0.9673	0.7121	0.8295	0.5981	0.6982	0.4834	0.2341
DSIFT	9.9257	0.9698	0.6999	0.8402	0.5791	0.6789	0.6732	6.5247
BF	9.8225	0.9794	0.7098	0.8415	0.7458	0.7124	0.6823	10.8973
CNN	9.8339	0.9785	0.7016	0.8432	0.6180	0.7345	0.6748	161.2210
SSDI	9.3226	0.9748	**0.7737**	0.8448	0.6253	**0.7984**	0.6768	72.3974
P-CNN	9.8426	0.9444	0.7315	0.8387	0.6192	0.7244	0.6438	**0.0633**
NSST-SCM	**9.9678**	**0.9895**	0.7389	**0.8572**	**0.7926**	0.7589	**0.6857**	60.7580

TABLE 3. Ealuation indexes of different fusion algorithms in figure 11.

The fusion algorithm	Q_C	Q_Y	Q_{PC}	Q_{NE}	Q_W	$Q_{AB/F}$	Q_{PL}	Time (s)
GFF	8.9562	0.9014	0.6825	0.8124	0.6275	0.8012	0.6951	0.7520
CST-GF	8.9975	0.9152	0.6851	0.8213	0.6321	0.8011	0.6932	9.7876
NSCT-PCNN	9.0124	0.9212	0.7142	0.7997	0.6452	0.7810	0.6887	262.8897
NSCT-SCM	9.0457	0.9320	0.6231	0.8314	0.6321	0.7802	0.7035	198.2276
NMF-DF	9.2543	0.8997	0.6852	0.7981	0.6221	0.7621	0.7021	10.4822
DCT	9.5617	0.9708	0.6932	0.8508	0.6115	0.7561	0.7087	0.2214
DSIFT	9.3063	0.9640	0.6631	0.8510	0.5985	0.7834	0.6887	6.8112
BF	9.9413	**0.9794**	0.8612	0.8517	0.6361	0.7724	0.7031	8.8971
CNN	8.5692	0.9778	0.6829	0.8508	0.6216	0.7677	0.7019	174.3321
SSDI	8.7982	0.9703	**0.9576**	0.8505	0.6354	0.7984	0.7081	68.0653
P-CNN	8.0156	0.9732	**0.9576**	0.8516	0.6107	0.8011	0.7074	**0.0433**
NSST-SCM	**9.5620**	**0.9794**	0.8998	**0.8610**	**0.6512**	**0.8089**	**0.7198**	58.5660

TABLE 4. Ealuation indexes of different fusion algorithms in figure 12.

The fusion algorithm	Q_C	Q_Y	Q_{PC}	Q_{NE}	Q_W	$Q_{AB/F}$	Q_{PL}	Time (s)
GFF	8.5425	0.9534	0.7365	0.8301	0.7041	0.7212	0.6698	0.6532
CST-GF	8.5682	0.9652	0.7451	0.8324	0.7052	0.7423	0.6732	10.3378
NSCT-PCNN	8.6425	0.9637	0.7485	0.8362	0.7021	0.6931	0.6798	256.5811
NSCT-SCM	8.6377	0.9721	0.7501	0.8356	0.6933	0.6925	0.6802	184.3227
NMF-DF	8.5243	0.9882	0.7498	0.8287	0.6534	0.7334	0.6823	10.2001
DCT	8.7827	0.9647	0.7548	0.8372	0.6876	0.7258	0.6927	0.2148
DSIFT	8.4681	0.9730	0.7154	0.8397	0.6721	0.6852	0.6898	0.5447
BF	8.9413	0.9688	0.7270	0.8369	0.6745	0.6936	0.6882	10.6313
CNN	8.5692	0.9608	0.7037	0.8381	0.7037	0.7356	0.6848	162.3370
SSDI	8.9759	0.9702	0.7933	0.8347	0.7027	0.7327	0.6725	70.9659
P-CNN	8.1169	0.9806	0.7896	0.8369	0.7045	0.7394	0.6819	**0.0299**
NSST-SCM	**8.9889**	**0.9889**	**0.7985**	**0.8499**	**0.7127**	**0.7423**	**0.6986**	63.6652

exist in FIGURE 10 (a), (b), (c) and (e). There are spots in the difference images of FIGURE 10 (f) and (k), and the information of the source images is not sufficiently extracted. The boundary content of the image is not well extracted in the FIGURE 10 (g-j). The fused image generated through our method has less artificial texture, more detail of source

TABLE 5. Ealuation indexes of different fusion algorithms in figure 13.

The fusion algorithm	Q_C	Q_Y	Q_{PC}	Q_{NE}	Q_W	$Q_{AB/F}$	Q_{PL}	Time (s)
GFF	6.3524	0.9032	0.6869	0.8368	0.5100	0.7524	0.7265	0.5346
CST-GF	6.3852	0.9056	0.6923	0.8357	0.4996	0.7605	0.7302	10.3354
NSCT-PCNN	6.4025	0.9024	0.6914	0.8349	0.5013	0.7046	0.7508	249.1143
NSCT-SCM	6.6528	0.9035	0.7027	0.8393	0.5017	0.7032	0.7403	187.7732
NMF-DF	5.9984	0.9018	0.6993	0.8317	0.5009	0.7648	0.7324	10.5116
DCT	**6.8808**	0.9024	0.7052	0.8411	0.5004	0.7128	0.7250	0.2449
DSIFT	6.2020	0.9120	0.7014	0.8408	0.5088	0.7132	0.7661	5.9340
BF	5.3070	0.9312	0.7032	0.8432	0.4984	0.7506	0.7649	10.0739
CNN	5.3140	0.9045	0.7037	0.8416	0.5012	0.7403	0.7483	181.1821
SSDI	6.1034	0.9148	0.7878	0.8396	0.4963	0.7574	0.7040	70.6119
P-CNN	5.8448	0.9372	0.7793	0.8403	0.5047	0.7448	0.7107	**0.0355**
NSST-SCM	6.4681	**0.9456**	**0.7889**	**0.8502**	**0.5101**	**0.7659**	**0.7665**	69.5524

TABLE 6. Ealuation indexes of different fusion algorithms in figure 14.

The fusion algorithm	Q_C	Q_Y	Q_{PC}	Q_{NE}	Q_W	$Q_{AB/F}$	Q_{PL}	Time (s)
GFF	8.6652	0.8995	0.7538	0.8321	0.7742	0.7914	0.7502	0.6532
CST-GF	8.6671	0.8854	0.7547	0.8337	0.7784	0.7928	0.7541	10.4452
NSCT-PCNN	8.7012	0.9026	0.7572	0.8378	0.7698	0.7309	0.7553	244.5211
NSCT-SCM	8.7053	0.9087	0.7602	0.8401	0.7805	0.7746	0.7622	189.3255
NMF-DF	8.6937	0.9223	0.7516	0.8363	0.7812	0.7834	0.7533	10.6554
DCT	8.9138	0.9538	0.7608	0.8399	0.7743	0.7502	0.7490	0.2148
DSIFT	8.8856	0.9633	0.7648	0.8434	0.7657	0.7689	0.7616	0.5447
BF	8.4273	**0.9648**	0.7616	0.8394	0.7713	0.7596	0.7649	10.6313
CNN	8.0747	0.9525	0.7559	0.8407	0.7869	0.7824	0.7483	162.3370
SSDI	8.1445	0.9583	**0.8136**	0.8426	0.7765	0.7922	0.7560	72.1620
P-CNN	8.0674	0.9406	0.8123	0.8341	0.7712	0.7877	0.7646	**0.0358**
NSST-SCM	**8.9325**	0.9617	0.8055	**0.8472**	**0.7871**	**0.7941**	**0.7728**	53.6652

images and better space continuity. Comparison of the difference images to get that our fused algorithm has the best fused image clarity and spatial continuity and the least artificial textures.

At the same time, we also use different evaluation indicators to show the performance of different algorithms. The highest value of each evaluation indicator is marked bold. We can draw from TABLE 2 that the proposed algorithm has the best performance in Q_C, Q_Y, Q_{NE}, Q_W and Q_{PL}. And the proposed algorithm has the best performance in Q_{PC} and $Q_{AB/F}$ except for SSID. That is contributed to SSID use depth information and non-local information of image.

Although compared to GFF and DCT, our algorithm has no advantage in terms of computational efficiency. In the overall evaluation index, our algorithm is effective and has good performance.

As we can see, in FIGURE 11 (a)-(l), our method has the best visual effect in all fusion methods. Comparison of the different images also reflects that our method has the best fused image clarity and spatial continuity, and the least artificial textures.

Besides the subjective visual appearance, TABLE 3 shows that the proposed algorithm has the best performance in Q_C, Q_Y, Q_{NE}, Q_W, $Q_{AB/F}$ and Q_{PL}, especially the Q_{PL} criterion, which means our algorithm has absolute priority in image processing to suppress artificial textures and preserve the details of original images. Though, the proposed algorithm has the smaller value in Q_{PC} than SSDI and P-CNN, it has higher value in Q_{PC} than others.

FIGURE 12 shows fused images by using twelve fused algorithms tested on group c. The same result as indicated in FIGURE 11, our algorithm is more advanced than others. The difference images in FIGURE 12. (c1-d2) have many artifacts, which show that NSCT-PCNN and NSCT-SCM cannot preserve all the details of source images. FIGURES 12 (b2) and (e2) show that the decision maps of CST-GF and NMF-DF have isolated point and artifacts. FIGURE 12 (a2) shows that GFF lead into block effect in fusion image. FIGURE 12 (f1-i2) does not distinguish

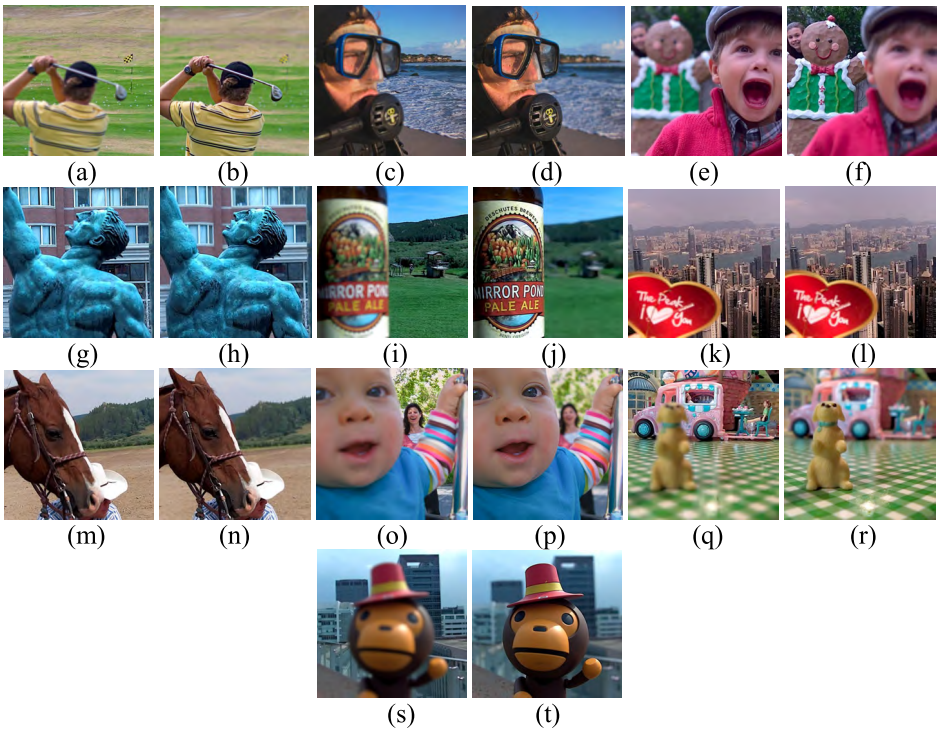

FIGURE 15. Different images from Lytro multi-focus dataset to fuse.

between focused and unfocused regions well at the boundary. It shows that the DCT, DFIFT, BF and CNN algorithms cannot make good use of the feature information of the images. FIGURE 12 (j1-k2) have a block effect near the boundary of the timepiece. It shows that SSDI and P-CNN have poor spatial continuity. And the algorithm designed in this paper can obtain more information of the original images while suppress block effect, artifacts and other useless image information much more effective.

Besides the subjective visual appearance, TABLE 4 shows that the proposed algorithm has the best performance in all of seven objective indicators, especially the Q_{NE} criterion and Q_{PC} criterion, which means our algorithm has absolute priority in image processing to preserve the details of original images and our algorithm also has better spatial continuity.

FIGURE 13 shows fused images by using twelve fused algorithms tested on group d. We can draw from the fusion results in FIGURE 13 that our algorithm performs better than other algorithms. Obviously, from FIGURE 13 (a2-d2), fusion images by GFF, CST-GF, NSCT-PCNN, and NSCT-SCM all lost much useful information of source images. FIGURE 13 (e1-i1) and (k1, k2) have artifacts in the texture portion of the bottom right corner of the clock. It shows that the NMF-DF, DCT, DFIFT, BF, CNN and P-CNN algorithms are not perfect in the fusion of detail features. There are significant discontinuities in FIGURE 13 (j1-j2). Compare FIGURE 13 (k) with FIGURE 13 (l), our algorithm has been performed better than NMF-DF in visual appearance. NSST-SCM can retain the texture information of source images and reduce artifacts much more effective.

From the TABLE 5, we can see that our algorithm has the best performance in Q_Y, Q_{PC}, Q_{NE}, Q_W, $Q_{AB/F}$ and Q_{PL}, which means our algorithm has absolute priority in image processing to suppress artificial textures and preserve the details of original images. Though, the proposed algorithm has the smaller value in Q_C than DCT and NSCT-SCM, it has higher value in Q_C than others. So, our algorithm can be considered as a robust multi-focus image fusion algorithm.

FIGURE 14 shows fused images by using twelve fused algorithms tested on group e. Obviously, from FIGURE 14 (a1-f1), fusion images by GFF, CST-GF, NMF-DF and DCT lost much useful information of source images. However, from FIGURE 14 (a2-f2), fusion images by NSCT-PCNN and NSCT-SCM lost much useful information of source images. As seen from FIGURE 14 (g, h, i, and k), the boundary portion of the fused images is too smooth. However, there is a noticeable artificial texture in FIGURE 14 (j). So, our algorithm NSST-SCM has been performed better than other methods in visual appearance.

Besides the subjective visual appearance, TABLE 3 shows that the proposed algorithm has the best performance in Q_C, Q_{NE}, Q_W, $Q_{AB/F}$ and Q_{PL}. And, the proposed algorithm just has slight smaller value in Q_Y and Q_{PC} than the highest one. Although the proposed algorithm

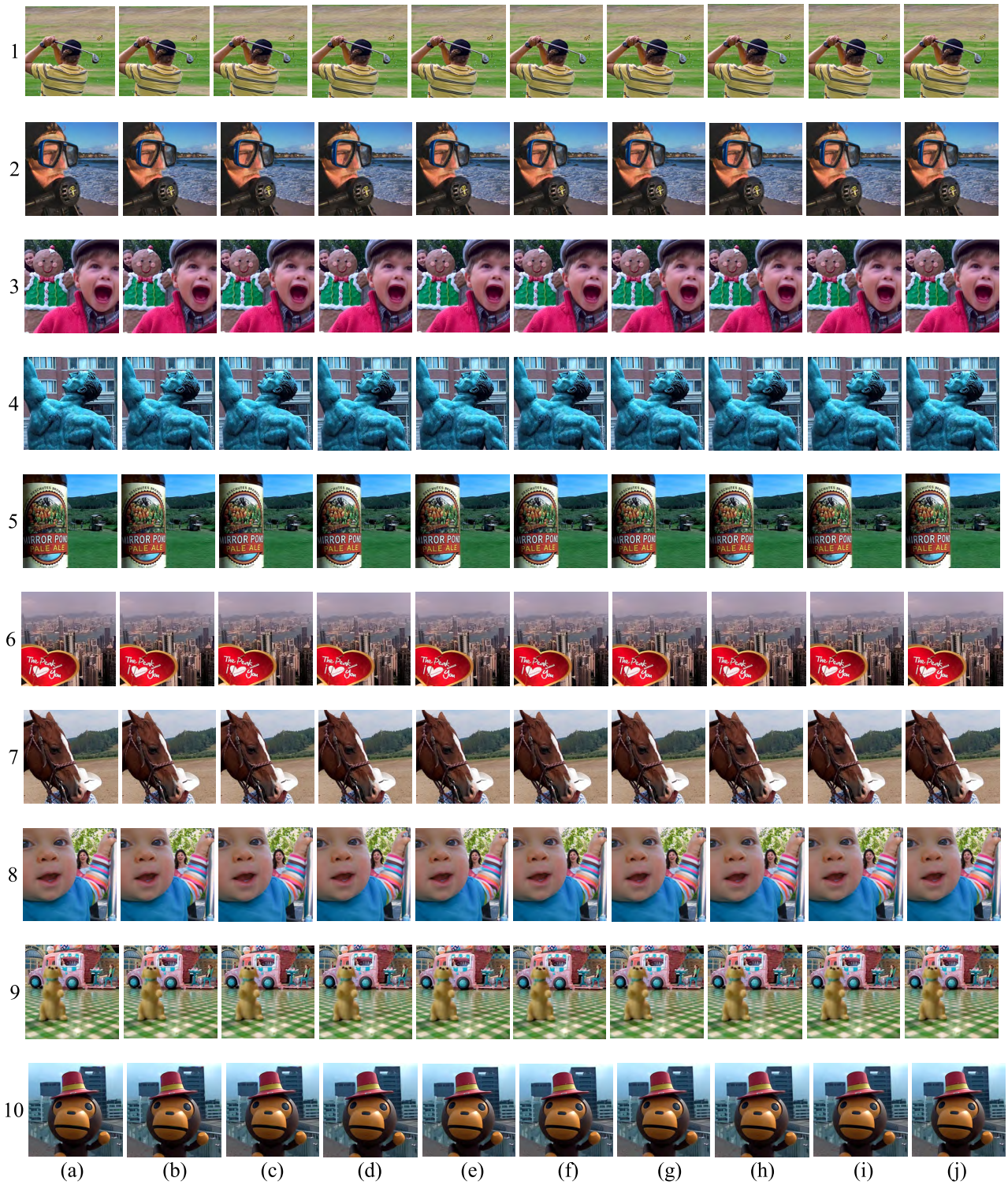

FIGURE 16. Fused results of ten pairs of source images using different methods. From left to right are the fused results of GFF, NMF-DF, NSCT-SC, DCT,DSIFT,BF,CNN,SSDI,P-CNN and NSST-CM.

is not the most efficient fused method, the experiment results show that our method also is competitive whether it is in terms of subjectively and objectively in fusion quality.

B. COMPARISON OF DIFFERENT ALGORITHMS IN COLOR IMAGES

In FIGURE 15, we give another ten pairs of multi-focus images from Lytro multi-focus dataset [45] to verify

TABLE 7. Ealuation indexes of different fusion algorithms in figure 16.1-5.

	Methods	Q_C	Q_Y	Q_{PC}	Q_{NE}	Q_W	$Q_{AB/F}$	Q_{PL}
Figure 16.1	GFF	8.0547	0.8702	0.7589	0.8414	0.8428	0.7208	0.6728
	NMF-DF	8.0536	0.8714	0.7657	0.8425	0.8437	0.7217	0.6724
	NSCT-SCM	8.0528	0.8734	0.7634	0.8417	0.8456	0.7236	0.6913
	DCT	8.0621	0.8757	0.7509	0.8409	0.8329	0.7225	0.6919
	DSIFT	8.0589	0.8652	0.7927	0.8441	0.8438	0.7312	0.6931
	BF	8.0758	0.8803	0.7935	0.8436	0.8346	0.7522	0.6735
	CNN	8.0769	0.8837	0.7938	0.8475	0.8336	0.7532	0.6746
	SSDI	**8.1221**	0.8891	0.8044	0.8388	0.8386	0.7541	0.6838
	P-CNN	8.0987	0.8675	**0.8052**	0.8357	0.8439	0.7428	0.6828
	NSST-SCM	8.0998	**0.8896**	0.7806	**0.8486**	**0.8487**	**0.7584**	**0.7014**
Figure 16.2	GFF	7.9928	0.9641	0.8223	0.8506	0.8347	0.7312	0.6985
	NMF-DF	7.9856	0.9621	0.8247	0.8514	0.8635	0.7325	0.6937
	NSCT-SCM	7.8978	0.9652	0.8256	0.8503	0.8321	0.7334	0.6941
	DCT	8.0225	0.9774	0.8173	**0.8515**	0.8431	0.7225	0.6946
	DSIFT	8.0678	0.9705	0.8159	0.8489	0.8435	0.7321	0.7021
	BF	8.1254	0.9536	0.7968	0.8475	0.8428	0.7522	0.7034
	CNN	**8.1452**	0.9528	0.7934	0.8482	0.8357	0.7532	0.7019
	SSDI	8.0655	0.9575	0.8231	0.8494	0.8339	0.7541	0.7114
	P-CNN	7.9986	0.9587	0.8199	0.8435	0.8396	0.7461	0.7148
	NSST-SCM	7.9964	**0.9782**	**0.8377**	0.8472	**0.8679**	**0.7557**	**0.7189**
Figure 16.3	GFF	9.0248	0.9028	0.7943	0.8356	0.8511	0.6991	0.7238
	NMF-DF	9.3730	0.9014	0.8357	0.8465	0.8524	0.6989	0.7216
	NSCT-SCM	9.4251	0.9052	**0.8541**	0.8375	0.8516	0.7103	0.7225
	DCT	9.3244	0.9035	0.8306	0.8421	0.8385	0.7114	0.7328
	DSIFT	8.3951	0.9087	0.8314	0.8342	0.8369	0.7123	0.7314
	BF	8.4710	0.9028	0.8354	0.8503	0.8432	0.6996	0.7343
	CNN	8.7147	0.9105	0.7996	0.8610	0.8532	0.7134	0.7327
	SSDI	8.8192	0.9156	0.8028	0.8546	0.8565	0.7119	0.7317
	P-CNN	9.0112	0.8997	0.8427	0.8321	**0.8578**	0.7154	0.7381
	NSST-SCM	**9.5021**	**0.9195**	0.8205	**0.8643**	0.8547	**0.7176**	**0.7405**
Figure 16.4	GFF	7.8872	0.9338	0.8115	0.8390	0.8293	0.7235	0.7405
	NMF-DF	8.2165	0.9366	0.8196	0.8477	0.8282	0.7217	0.7410
	NSCT-SCM	8.4635	0.9325	0.8084	0.8391	0.8261	0.7276	0.7421
	DCT	8.4393	0.9374	0.8209	0.8454	0.8391	0.7247	0.7409
	DSIFT	8.3315	0.9258	0.8094	0.8339	0.8253	0.7533	0.7613
	BF	8.4532	0.9287	0.8068	0.8525	0.8265	0.7518	0.7606
	CNN	7.8354	0.9418	0.8214	**0.8627**	0.8278	0.7529	0.7487
	SSDI	7.9982	0.9421	0.8230	0.8557	0.8387	0.7534	0.7615
	P-CNN	8.0242	0.9435	0.8226	0.8335	0.8408	0.7498	0.7611
	NSST-SCM	**8.5042**	**0.9480**	**0.8245**	0.8474	**0.8409**	**0.7567**	**0.7641**
Figure 16.5	GFF	**8.9114**	0.9664	0.9201	0.8388	0.7991	0.7321	0.7033
	NMF-DF	8.4035	0.9587	0.9206	0.8480	0.7982	0.7316	0.7013
	NSCT-SCM	8.4210	0.9604	0.9214	0.8392	0.8013	0.7313	0.7027
	DCT	8.4774	0.9624	0.9221	0.8452	0.8007	0.7306	0.7034
	DSIFT	8.5223	0.9632	0.9234	0.8338	0.8024	0.7325	0.7128
	BF	8.4522	0.9558	0.9174	0.8398	0.7989	0.7114	0.7153
	CNN	8.4502	0.9529	0.9088	0.8527	0.8028	0.7538	0.7119
	SSDI	8.5410	0.9607	0.9079	**0.8624**	0.8097	0.7541	0.7089
	P-CNN	8.8813	0.9625	0.9306	0.8577	0.8136	0.7463	0.7176
	NSST-SCM	8.5664	**0.9698**	**0.9438**	0.8597	**0.8186**	**0.7574**	**0.7191**

the algorithm. The comparison algorithms are GFF, NMF-DF, NSCT-SCM, DCT, DSIFT, BF, CNN, SSDI, P-CNN and NSST-SCM. The fusion results of the multi-focus images of different algorithms are shown in FIGURE 16.

FIGURE 16 shows fused images by using ten fused algorithms tested on FIGURE 15. The last line images in FIGURE 16 of the different scenes are the fusion result of our algorithm. From the fusion results, we can find that our fusion algorithm still has strong competitiveness. GFF performs the fusion of the source images by filtering the weight map obtained. Therefore, this method may produce artifacts. As shown in FIGURE 16.1 (a), there is a noticeable artificial texture at the starting position. The text on the ''soda bottle'' in FIGURE 16.5 (a) has artifacts. The fusion result obtained by the NMF-DF and NSCT-SCM algorithms has a block effect. The ''face'' portion of FIGURE 16.8 (b) and the ''high-rise'' area of FIGURE 16.10 (c) have blurred artifact. In the DCT method, the fusion weight map is obtained by the scale transformation coefficient, and there is an area of erroneous selection. Defocus areas exist in the boundary regions as shown in FIGURES 16.9 (d) and 16.7 (d). In the process of determining the focus area, the DSIFT algorithm may have unregistered images, which will seriously affect the quality of the fused image. In FIGURE 16.4 (e), the

TABLE 8. Ealuation indexes of different fusion algorithms in figure 16.6-10.

	Methods	Q_C	Q_Y	Q_{PC}	Q_{NE}	Q_W	$Q_{AB/F}$	Q_{PL}
Figure 16.6	GFF	8.3361	0.8916	0.7993	0.8346	0.8385	0.7325	0.6772
	NMF-DF	8.3128	0.8925	0.7987	0.8456	0.8427	0.7331	0.6789
	NSCT-SCM	8.2134	0.8846	0.7965	0.8372	0.8516	0.7289	0.6793
	DCT	**8.4256**	0.8876	0.8276	0.8312	0.8402	0.7296	0.6857
	DSIFT	8.4117	0.8937	0.8223	0.8530	0.8419	0.7415	0.6883
	BF	8.3469	0.8902	0.8215	**0.8611**	0.7998	0.7511	**0.7135**
	CNN	8.3287	0.8918	0.8127	0.8542	0.7986	0.7506	0.7129
	SSDI	8.3411	0.8909	0.8048	0.8415	0.8301	0.7379	0.7058
	P-CNN	8.3405	0.8865	0.8079	0.8442	0.8305	0.7364	0.7114
	NSST-SCM	8.4021	**0.8933**	**0.8287**	0.8509	**0.8552**	**0.7524**	**0.7135**
Figure 16.7	GFF	8.3123	0.9088	0.9032	0.8329	0.8345	0.7341	0.7225
	NMF-DF	8.3041	0.9076	0.9015	0.8447	0.8419	0.7523	0.7213
	NSCT-SCM	7.9150	0.9035	0.9152	0.8336	**0.8506**	0.6994	0.6782
	DCT	7.9087	0.9021	0.9143	0.8417	0.8297	0.7028	0.6849
	DSIFT	8.2256	0.9057	0.9088	0.8527	0.8413	0.7346	0.7228
	BF	8.2332	0.9110	0.9076	0.8615	0.8094	0.7452	0.6889
	CNN	7.9279	0.9115	0.9503	0.8632	0.8083	0.7431	0.6973
	SSDI	8.3465	**0.9317**	0.9112	0.8427	0.8425	0.7276	0.7315
	P-CNN	8.3398	0.9192	0.9127	0.8453	0.8376	0.7255	0.7224
	NSST-SCM	**8.3476**	0.9118	**0.9604**	**0.8672**	0.8413	**0.7585**	**0.7344**
Figure 16.8	GFF	9.0825	0.9501	0.8372	0.8319	0.8237	0.7071	0.7215
	NMF-DF	9.1063	0.9513	0.8363	0.8407	0.8324	0.7049	0.7223
	NSCT-SCM	9.1318	0.9525	0.8319	0.8346	0.8413	0.7283	0.6841
	DCT	9.0779	**0.9543**	0.8357	0.8423	0.8285	0.7231	0.6883
	DSIFT	8.9685	0.9311	0.8541	0.8541	0.8415	0.7421	0.7239
	BF	8.6974	0.9318	0.8524	**0.8613**	0.8099	0.7416	0.6852
	CNN	8.7425	0.9324	0.8374	0.8526	0.7994	0.7431	0.6943
	SSDI	8.7353	0.9516	0.8418	0.8471	0.8361	0.7423	0.7099
	P-CNN	9.1145	0.9537	0.8506	0.8342	0.8359	0.7411	0.7093
	NSST-SCM	**9.1387**	0.9509	**0.8571**	0.8478	**0.8462**	**0.7504**	**0.7248**
Figure 16.9	GFF	8.2309	0.9611	0.8804	0.8215	0.8390	0.7311	0.7211
	NMF-DF	8.2876	0.9166	0.8815	0.8423	0.8425	0.7088	0.7235
	NSCT-SCM	8.2541	0.9135	0.8923	0.8233	**0.8514**	0.7286	0.7228
	DCT	8.5018	0.9627	0.8942	0.8329	0.8416	0.7184	0.7078
	DSIFT	8.5342	0.9441	0.8871	0.8547	0.8369	0.7192	0.7065
	BF	8.7116	0.9446	0.8901	**0.8652**	0.7985	0.7169	0.7168
	CNN	8.7238	0.9433	0.8954	0.8578	0.8092	0.7245	0.7356
	SSDI	8.4992	0.9618	0.8736	0.8391	0.8381	0.7236	0.7614
	P-CNN	8.4571	0.9627	0.8825	0.8436	0.8348	0.7233	0.7502
	NSST-SCM	**8.7428**	**0.9677**	**0.8972**	0.8452	0.8473	**0.7413**	**0.7672**
Figure 16.10	GFF	7.9533	0.9127	0.9586	0.8375	0.8258	0.7412	0.7221
	NMF-DF	8.0672	**0.9686**	0.9537	0.8446	0.8376	0.7405	0.7223
	NSCT-SCM	8.0197	0.9635	0.8825	0.8385	**0.8543**	0.7516	0.6996
	DCT	8.0186	0.9089	0.9348	0.8457	0.8279	0.7465	0.6993
	DSIFT	7.9984	0.9078	0.9519	0.8542	0.8317	0.7428	0.7311
	BF	8.1227	0.9206	0.9432	0.8639	0.8052	0.7536	0.6987
	CNN	8.1552	0.8996	0.9426	0.8572	0.8099	0.7449	0.6992
	SSDI	8.1178	0.9237	0.9518	0.8341	0.8345	0.7504	0.7316
	P-CNN	8.0927	0.9144	0.9534	0.8384	0.8327	0.7515	0.7303
	NSST-SCM	**8.1575**	0.9188	**0.9592**	**0.8729**	0.8414	**0.7553**	**0.7348**

"arm" section has a blurring effect that affects the visual effect. At the same time, artifacts appear on the edge of the images. In the process of generating the weight map, the BF algorithm only generates weight distribution in the boundary part. This causes the distinction between focus and non-focus to appear as a texture. Artifacts appear in the frame portion of FIGURE 16.1 (f). There are also obvious human factors in FIGURE 16.9 (f). In the CNN and P-CNN methods, the blocking effect is reduced by training the classification labels to distinguish different degrees of focus. In FIGURES 16.10 (g) and (i), defocus appears near the "high building". In the vicinity of the "nose" in FIGURES 16.7 (g), a defocused block appears. In the SSDI method, the information features of the source images cannot be fully extracted, and the fused image has poor visual effect. As in FIGURES 16.3 (h) and 16.5 (h), the visual effect of the fusion results is blurred.

It can be seen from the data obtained from the objective evaluation indicators of TABLE 7 and TABLE 8 that the proposed algorithm is better than others among most of the seven objective evaluation indicators.

C. ALGORITHM DECISION MAP

In order to prove the efficiencies of the proposed algorithm, we compare the decision maps of different algorithms. By this way, people can see the edges and contour features of the

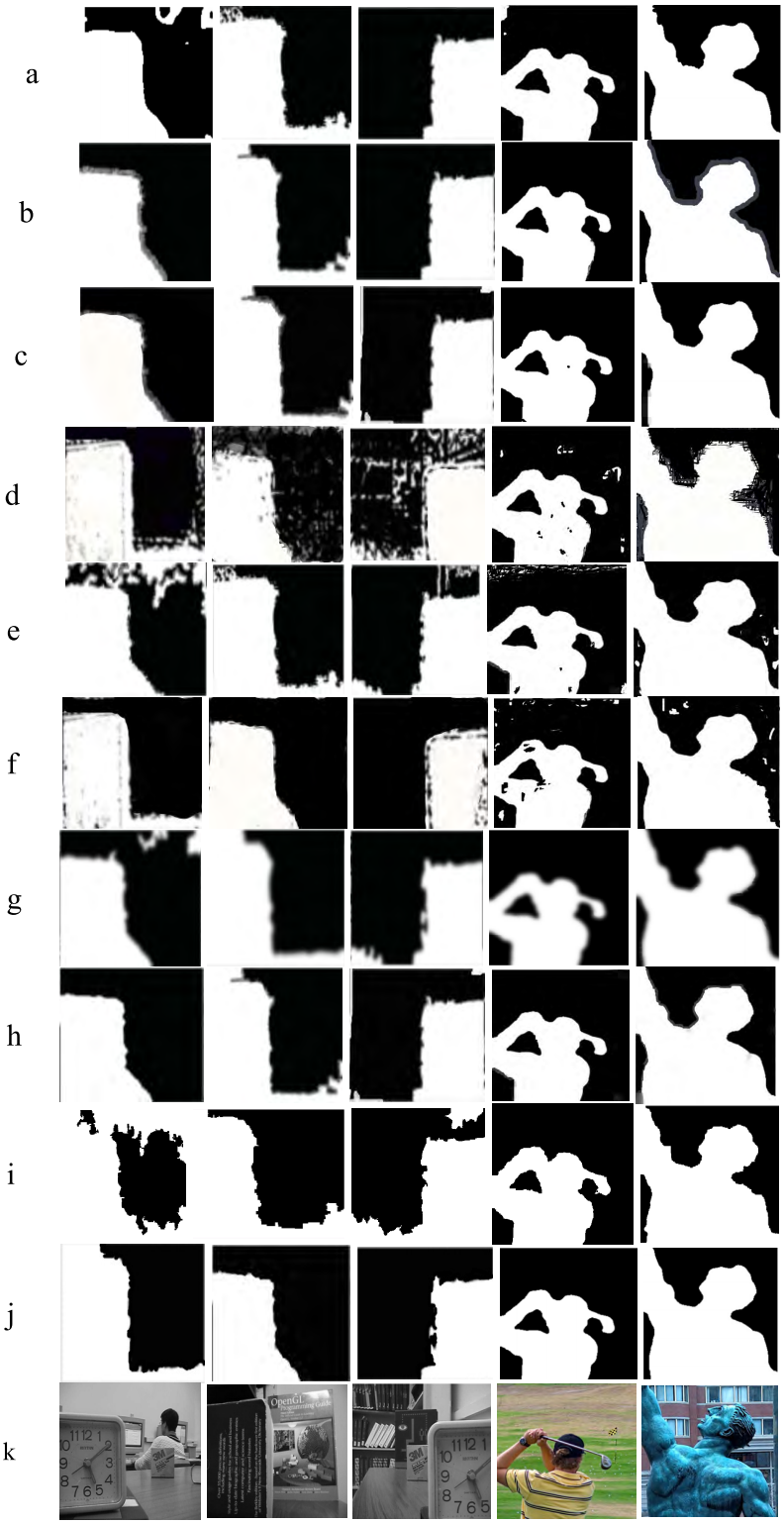

FIGURE 17. The decision map obtained by GFF, NMF-DF, NSCT-SC, DCT, DSIFT,BF,CNN,SSDI, P-CNN and NSST-CM.

image more clearly. We use five pairs of source images as comparisons, from top to bottom are the decision maps of different algorithms, the last line is the fused images, and the final result is shown in FIGURE 17. In the process of generating the decision maps, regards the value from the source image A or B in the decision graph as 0 or 1. As can be seen from the decision diagram, the model we designed can effectively segment most pixels. Therefore, the model

we designed is effective. The last line in the figure is the fused images produced by the algorithm decision graph in this paper.

The experimental results show that the proposed algorithm can improve the accuracy of the fused image, keep the details and texture of the source image with less artificial texture features, and also has better computational efficiency. Furthermore, this algorithm is easy to implement and has achieved high efficiency in the field of image fusion.

VI. CONCLUSIONS

This paper designs a new image fusion algorithm which is based on dual-SCM in NSST domain and difference images between the basic fused image and source images. Through the dual-SCM in the NSST domain, the basic fused image is produced. Then, we use EOG of difference images to refine the basic fused image by combining average filter and median filter. The proposed algorithm in this paper can produce clearer images, better visual effects and extract the detailed features of images more effectively. Compared with the current popular deep learning processing algorithm, the training time of the data set is effectively reduced, and the proposed algorithm does not need to train, which can simple the task of image fusion. The experimental results show that our method is superior to most of advanced image processing algorithms and is a satisfactory image fusion algorithm in the application field.

ACKNOWLEDGMENT

Some of the images adopted in experiments are downloaded from the website of http: //www.imagefusion.org and https://mansournejati.ece.iut.ac.ir/content/lytro-multi-focus-dataset. We also thank Dr. Qu, Dr. Kang, Dr. Zhang Dr. Xiao and Dr. Liu for their shared codes of image fusion. We also thank the Editor and Reviewers for the efforts made in processing this submission and we are particularly grateful to the reviewers for their constructive comments and suggestions which help us improve the quality of this paper.

REFERENCES

[1] M. S. Farid, A. Mahmood, and S. A. Al-Maadeed, "Multi-focus image fusion using content adaptive blurring," *Inf. Fusion*, vol. 45, pp. 96–112, Jan. 2019.

[2] S. Li, X. Kang, L. Fang, J. Hu, and H. Yin, "Pixel-level image fusion: A survey of the state of the art," *Inf. Fusion*, vol. 33, pp. 100–112, Jun. 2017.

[3] W. Huang and Z. Jing, "Evaluation of focus measures in multi-focus image fusion," *Pattern Recognit. Lett.*, vol. 28, no. 4, pp. 493–500, 2007.

[4] Y. Jia, "Fusion of landsat TM and SAR images based on principal component analysis," *Remote Sens. Technol. Appl.*, vol. 13, no. 1, pp. 46–49, Mar. 1998.

[5] Y. Yang *et al.*, "Multi-focus image fusion via clustering PCA based joint dictionary learning," *IEEE Access*, vol. 5, pp. 16985–16997, 2017.

[6] S. Li, X. Kang, and J. Hu, "Image fusion with guided filtering," *IEEE Trans. Image Process.*, vol. 22, no. 7, pp. 2864–2875, Jul. 2013.

[7] D. Guo, J. Yan, and X. Qu, "High quality multi-focus image fusion using self-similarity and depth information," *Opt. Commun.*, vol. 338, pp. 138–144, Mar. 2015.

[8] M. R. Abuturab, "Multiple color-image fusion and watermarking based on optical interference and wavelet transform," *Opt. Lasers Eng.*, vol. 89, pp. 47–58, Feb. 2017.

[9] P. Geng, M. Huang, S. Liu, J. Feng, and P. Bao, "Multifocus image fusion method of Ripplet transform based on cycle spinning," *Multimedia Tools Appl.*, vol. 75, no. 17, pp. 10583–10593, Sep. 2016.

[10] Y. Dongsheng, H. Shaohai, L. Shuaiqi, M. Xiaole, and S. Yuchao, "Multi-focus image fusion based on block matching in 3D transform domain," *J. Syst. Eng. Electron.*, vol. 29, no. 2, pp. 415–428, Apr. 2018.

[11] X. Luo, Z. Zhang, B. Zhang, and X. Wu, "Image fusion with contextual statistical similarity and nonsubsampled shearlet transform," *IEEE Sensors J.*, vol. 17, no. 6, pp. 1760–1771, Mar. 2017.

[12] L. Chen, J. Li, and C. L. P. Chen, "Regional multifocus image fusion using sparse representation," *Opt. Express*, vol. 21, no. 4, pp. 5182–5197, 2013.

[13] K. Wang, G. Qi, Z. Zhu, and Y. Chai, "A novel geometric dictionary construction approach for sparse representation based image fusion," *Entropy*, vol. 19, no. 7, pp. 306–323, Jun. 2017.

[14] M. Amin-Naji, P. Ranjbar-Noiey, and A. Aghagolzadeh, "Multi-focus image fusion using singular value decomposition in DCT domain," in *Proc. 10th Iranian Conf. Mach. Vis. Image Process. (MVIP)*, Nov. 2017, pp. 45–51.

[15] X.-B. Qu, J.-W. Yan, H.-Z. Xiao, and Z.-Q. Zhu, "Image fusion algorithm based on spatial frequency-motivated pulse coupled neural networks in nonsubsampled contourlet transform domain," *Acta Automatica Sinica*, vol. 34, no. 12, pp. 1508–1514, Dec. 2008.

[16] P. Geng, Z. Wang, Z. Zhang, and Z. Xiao, "Image fusion by pulse couple neural network with shearlet," *Proc. SPIE*, vol. 51, Jun. 2012, Art. no. 067005.

[17] N. Wang, Y. Ma, W. Wang, and K. Zhan, "Multifocus image fusion based on nonsubsampled contourlet transform and spiking cortical model," *Neural Netw. World*, vol. 25, no. 6, pp. 623–639, Nov. 2015.

[18] S. Liu, S. Hu, and Y. Xiao, "Image separation using wavelet-complex shearlet dictionary," *J. Syst. Eng. Electron.*, vol. 25, no. 2, pp. 314–321, Apr. 2014.

[19] G. Easley, D. Labate, and W.-Q. Lim, "Sparse directional image representations using the discrete shearlet transform," *Appl. Comput. Harmon. Anal.*, vol. 25, no. 1, pp. 25–46, Jul. 2008.

[20] W.-Q. Lim, "The discrete shearlet transform: A new directional transform and compactly supported shearlet frames," *IEEE Trans. Image Process.*, vol. 19, no. 5, pp. 1166–1180, May 2010.

[21] S. Q. Liu, S. H. Hu, Y. Xiao, and Y. Li An, "Bayesian shearlet shrinkage for SAR image de-noising via sparse representation," *Multidimensional Syst. Signal Process.*, vol. 25, no. 4, pp. 683–701, Oct. 2014.

[22] Y. Sun, S. Hu, S. Liu, and W. Sun, "A novel multi-focus image fusion algorithm based on NSST-FRFT," in *Proc. 12th Int. Conf. Signal Process. (ICSP)*, Oct. 2014, pp. 780–783.

[23] N. Wang, Y. Ma, and K. Zhan, "Spiking cortical model for multifocus image fusion," *Neurocomputing*, vol. 130, pp. 44–51, Apr. 2014.

[24] X. Jin *et al.*, "Remote sensing image fusion algorithm based on S-PCNN and two-dinensional stationary wavelet transform," *Laser Optoelectron. Progr.*, vol. 52, pp. 101001-1–101001-6, 2015.

[25] H. Shaohai, Y. Dongsheng, L. Shuaiqi, and M. Xiaole, "Block-matching based multimodal medical image fusion via PCNN with SML," in *Proc. IEEE 13th Int. Conf. Signal Process. (ICSP)*, Nov. 2017, pp. 13–18.

[26] K. Zhan, H.-J. Zhang, Y.-de Ma, L. Liu, and L. Tian, "Image processing using intersecting cortical model," *J. Beijing, China Univ. Posts Telecommun.*, vol. 32, no. 4, pp. 40–45, 2009.

[27] K. Zhan, H. Zhang, and Y. Ma, "New spiking cortical model for invariant texture retrieval and image processing," *IEEE Trans. Neural Netw.*, vol. 20, no. 12, pp. 1980–1986, Dec. 2009.

[28] N. Wang, Y. Ma, K. Zhan, and Y. Min, "Multimodal medical image fusion framework based on simplified PCNN in nonsubsampled contourlet transform domain," *J. Multimedia*, vol. 8, no. 3, pp. 270–276, Jun. 2013.

[29] S. Liu, J. Zhao, and M. Shi, "Medical image fusion based on rolling guidance filter and spiking cortical model," *Comput. Math. Methods Med.*, vol. 2015, May 2015, Art. no. 156043.

[30] T. Xiang, L. Yan, and R. Gao, "A fusion algorithm for infrared and visible images based on adaptive dual-channel unit-linking PCNN in NSCT domain," *Infr. Phys. Technol.*, vol. 69, pp. 53–61, Mar. 2015.

[31] Y. Zhang, L. Chen, J. Jia, and Z. Zhao, "Multi-focus image fusion based on non-negative matrix factorization and difference images," *Signal Process.*, vol. 105, pp. 84–97, Dec. 2014.

[32] C. Du and S. Gao, "Image segmentation-based multi-focus image fusion through multi-scale convolutional neural network," *IEEE Access*, vol. 5, pp. 15750–15761, 2017.

[33] Y. Liu, X. Chen, H. Peng, and Z. F. Wang, "Multi-focus image fusion with a deep convolutional neural network," *Inf. Fusion*, vol. 36 pp. 191–207, Jul. 2017.
[34] H. Tang, B. Xiao, W. Li, and G. Wang, "Pixel convolutional neural network for multi-focus image fusion," *Inf. Sci.*, vols. 433–434, pp. 125–141, Apr. 2017.
[35] X. Guo, R. Nie, J. Cao, D. Zhou, and W. Qian, "Fully convolutional network-based multifocus image fusion," *Neural Comput.*, vol. 30, no. 7, pp. 1775–1800, Jul. 2018.
[36] Y. Liu, X. Chen, Z. Wang, Z. J. Wang, R. K. Ward, and X. Wang, "Deep learning for pixel-level image fusion: Recent advances and future prospects," *Inf. Fusion*, vol. 42, pp. 158–173, Jul. 2018.
[37] R. Wang, Y. Wu, M. Ding, and X. Zhang, "Medical image fusion based on spiking cortical model," *Proc. SPIE*, vol. 8676, Mar. 2013, Art. no. 867610.
[38] S. Liu, M. Shi, Z. Zhu, and J. Zhao, "Image fusion based on complex-shearlet domain with guided filtering," *Multidimensional Syst. Signal Process.*, vol. 28, no. 1, pp. 207–224, Jan. 2017.
[39] Y. Chen and R. S. Blum, "A new automated quality assessment algorithm for image fusion," *Image Vis. Comput.*, vol. 27, no. 10, pp. 1421–1432, Sep. 2009.
[40] J. Zhao, R. Laganière, and Z. Liu, "Performance assessment of combinative pixel-level image fusion based on an absolute feature measurement," *Int. J. Innov. Comput., Inf. Control*, vol. 3, no. 6, pp. 1433–1447, Dec. 2007.
[41] Z. Liu, E. Blasch, Z. Xue, J. Zhao, R. Laganiere, and W. Wu, "Objective assessment of multiresolution image fusion algorithms for context enhancement in night vision: A comparative study," *IEEE Trans. Pattern Anal. Mach. Intell.*, vol. 34, no. 1, pp. 94–109, Jan. 2012.
[42] M. Amin-Naji and A. Aghagolzadeh, "Multi-focus image fusion in DCT domain using variance and energy of Laplacian and correlation coefficient for visual sensor networks," *J. AI Data Mining*, vol. 6, no. 2, pp. 233–250, 2018.
[43] Y. Liu, S. Liu, and Z. Wang, "Multi-focus image fusion with dense SIFT," *Inf. Fusion*, vol. 23, pp. 139–155, May 2015.
[44] Y. Zhang, X. Bai, and T. Wang, "Boundary finding based multi-focus image fusion through multi-scale morphological focus-measure," *Inf. Fusion*,vol. 35, pp. 81–101, May 2017.
[45] M. Nejati, S. Samavi, and S. Shirani, "Multi-focus image fusion using dictionary-based sparse representation," *Inf. Fusion*, vol. 25, pp. 72–84, Sep. 2015.

SHUAIQI LIU received the B.S. degree from the Department of Information and Computer Science, Shandong University of Science and Technology, in 2009, and the Ph.D. degree from the Institute of Information Science, Beijing Jiaotong University, in 2014. From 2016 to 2017, he was a Visiting Scholar with Ottawa University. He is currently an Associate Professor with the College of Electronic and Information Engineering, Hebei University. His research interests include image processing and signal processing.

JIE WANG received the B.S. degree from the School of Industry and Commerce, Hebei University, in 2017, where she is currently pursuing the B.Eng. degree with the College of Electronic and Information Engineering. Her research interest includes image processing.

YUCONG LU received the B.S. degree from the College of Electronic and Information Engineering, Hebei University, in 2016, where she is currently pursuing the B.Eng. degree. Her research interests include image de-noising, software development, and image fusion.

HAILIANG LI received the M.Sc. degree from the Department of Automation, Xiamen University, China, in 2004. He is currently puruing the Ph.D. degree with The Hong Kong Polytechnic University. He is currenlty an Algorithm Software Engineer with Hong Kong Applied Science and Technology Research Institute Company Limited (ASTRI). His work is related to image processing and machine learning. His research interest includes image super-resolution.

JIE ZHAO received the B.S. and M.S. degrees from the Department of Computer Science, Hebei University, in 1992 and 1995, respectively, and the Ph.D. degree from the Department of Electronic Engineering, Hebei University of Technology, in 2008. He is currnetly a Visitor and a Professor with the College of Electronic and Information Engineering, Hebei University. He is also the Dean of the College of Electronic and Information Engineering. His research interests include signal processing and image processing.

ZHIHUI ZHU received the B.S. and M.S. degrees from the Department of Communications Engineering, Zhejiang University of Technology, and the Ph.D. degree from the Colorado School of Mines. He currently holds a Postdoctoral position at Johns Hopkins University, USA. His research interests include signal processing using sparse, low-dimensional signal models, and low-rate signal sensing and acquisition.